

Infrared Properties of Close Pairs of Galaxies

Margaret J. Geller

*Smithsonian Astrophysical Observatory,
60 Garden St., Cambridge, MA 02138*

mgeller@cfa.harvard.edu

Scott J. Kenyon

*Smithsonian Astrophysical Observatory,
60 Garden St., Cambridge, MA 02138*

skenyon@cfa.harvard.edu

Elizabeth J. Barton

*Department of Physics and Astronomy, University of California Irvine,
4154 Frederick Reines Hall, Irvine, CA 92697*

ebarton@uci.edu

Thomas H. Jarrett

*Infrared Processing and Analysis Center,
Spitzer Science Center, Jet Propulsion Laboratory,
California Institute of Technology, Pasadena, CA 91125*

jarrett@ipac.caltech.edu

Lisa J. Kewley

*Institute for Astronomy, University of Hawaii,
2680 Woodlawn Drive, Manoa, HI 96822*

kewley@ifa.hawaii.edu

ABSTRACT

We discuss spectroscopy and infrared photometry for a complete sample of ~ 800 galaxies in close pairs objectively selected from the CfA2 redshift survey. We use 2MASS to compare near infrared color-color diagrams for our sample with

the Nearby Field Galaxy Sample and with a set of IRAS flux-limited pairs from Surace et al. We construct a basic statistical model to explore the physical sources of the substantial differences among these samples. The model explains the spread of near infrared colors and is consistent with a picture where central star formation is triggered by the galaxy-galaxy interaction before a merger occurs. For 160 galaxies we report new, deep JHK photometry within our spectroscopic aperture and we use the combined spectroscopic and photometric data to explore the physical conditions in the central bursts. We find a set of objects with $H-K \geq 0.45$ and with a large F_{FIR}/F_H . We interpret the very red $H-K$ colors as evidence for 600–1000K dust within compact star-forming regions, perhaps similar to super-star clusters identified in individual well-studied interacting galaxies. The galaxies in our sample are candidate “hidden” bursts or, possibly, “hidden” AGN. Over the entire pair sample, both spectroscopic and photometric data show that the specific star formation rate decreases with the projected separation of the pair. The data suggest that the near infrared color-color diagram is also a function of the projected separation; all of the objects with central near infrared colors indicative of bursts of star formation lie at small projected separation.

Subject headings: galaxies:interacting, galaxies:photometry, galaxies:starburst

1. INTRODUCTION

Larson & Tinsley (1978) first recognized the close connection between galaxy-galaxy interactions and star formation. They suggested that this relationship is a fundamental ingredient of galaxy formation and evolution. Studies of individual interacting systems and of statistical samples of close pairs in the local universe have confirmed and refined the initial results (e.g. Kennicutt & Keel 1984; Kennicutt et al. 1987; Jones & Stein 1989; Sekiguchi & Wolstencroft 1992; Keel 1993; Liu & Kennicutt 1995a,b; Keel 1996; Donzelli & Pastoriza 1997; Barton, Geller, & Kenyon 2000 (BGK hereafter); Barton Gillespie, Geller, & Kenyon (2003; BGK2 hereafter); Lambas et al. 2003; Allam et al. 2004; Alonso et al. 2004; Nikolic et al. 2004). Examinations of the universe at high redshift underscore the importance of interactions in molding the evolution of galaxies (e.g. Patton et al. 2002; Conselice et al. 2004; Lin et al. 2004; Papovich et al. 2005; Bell et al. 2006).

The connection between interacting pairs of galaxies and star formation is now well established observationally and there is a promising correspondence between the predictions of simulations and the properties of well-defined samples of close pairs. The data are consistent with a burst of star formation triggered by a close galaxy-galaxy interaction; the burst

continues and ages as the galaxies move apart (Mihos et al. 1991; Mihos & Hernquist 1996; BGK, BGK2, Lambas et al. 2003; Nikolic et al. 2004). The primary feature of the data is an anti-correlation between the projected separation of a pair on the sky and measures of the normalized star formation rate. This anti-correlation suggests a dependence of the burst strength and probably burst age on the separation of the galaxy pair (BGK2).

Here we focus on near infrared observations of close pairs of galaxies in the full BGK sample with attention to the distinctive features of infrared emission possibly associated with the interaction. The literature contains detailed near infrared observations of famous individual interacting galaxy pairs (e.g. Lopez-Sanchez et al. 2004) and a few optical-infrared imaging surveys of small objectively selected samples of close pairs. Bushouse & Werner (1990) imaged a sample of 22 interacting galaxies. In their sample, the nuclei are redder than the outer regions by ~ 0.4 and 0.9 mag in J-K and R-K, respectively. They attribute the color gradient mostly to an increase in the amount of dust in the nuclear regions and argue that the infrared colors are unaffected by dust emission. Cutri and McAlary (1985) carried out small aperture photometry of a larger sample of pairs. They concluded that a larger fraction of interacting than non-interacting galaxies have J-K and H-K colors outside the normal range. Giuricin et al. (1993) used a compendium of data from the literature to investigate the effect of interactions on the near infrared properties of spiral galaxies. In contrast with Bushouse and Werner (1990), they concluded that apparently interacting galaxies have H-K and K-L excesses indicative of thermal emission from hot dust probably related to star formation induced by the interaction. We use our spectroscopy and matched small aperture photometry along with 2MASS photometry to revisit these issues in a much larger dataset of nearly 800 galaxies in close pairs and n-tuples.

In the far infrared, IRAS observations still yield the largest datasets for consideration of the properties of galaxy-galaxy interactions as a function of observable descriptors of the pair (see, for example, Goto 2005). Telesco, Wolstencroft & Done (1988) compiled IRAS observations of pairs selected from the catalog of Arp & Madore (1987) and resolved by IRAS. In their set of 93 pairs of comparable luminosity, they find that pairs with the highest far infrared color temperature have the smallest projected separation on the sky. They concluded that interactions measurably enhance the intensity or efficiency of star formation. Bushouse et al. (1988) reached similar conclusions based on IRAS observations of a sample of pairs selected on the basis of optical morphology.

Recently Surace, Sanders & Mazzarella (2004; SSM hereafter) used HIRES image reconstruction to resolve the IRAS emission at 12, 25, 60, and $100\text{ }\mu\text{m}$ for 106 interacting galaxy systems where the galaxies are separated by less than three average galaxy diameters. The sample has a flux limit at $60\text{ }\mu\text{m}$ of 5.24 Jy . We use their sample to provide a context for

discussion of the generally unresolved IRAS detections in our sample. Neither the SSM or BGK samples contain any ultraluminous infrared galaxies.

The complexity of the underlying sources of emission in the near infrared has probably been a disincentive to investigating pairs in this spectral range. With current data it remains difficult to disentangle the effects of reddening and thermal dust emission at several temperatures. Photometry at L together with spatially resolved photometry of large samples at longer wavelengths are necessary for clearer understanding of these issues. Currently available data are, however, adequate to demonstrate the promise of the infrared for probing the galaxy-galaxy merger process and the links between galaxy-galaxy interactions and star formation.

Here we compile the largest sample to date of near infrared colors of galaxy pairs. The data we consider include 2MASS JHK_s photometry for 791 galaxies in the BGK sample and our own deeper JHK small aperture photometry for a subsample of 160 BGK galaxies. We also use IRAS detections and upper limits for the entire BGK sample as a marker of the relationship between galaxy-galaxy interactions, star formation, and thermal emission from hot dust in these systems. We use our optical spectra and infrared colors measured through the same aperture to investigate basic properties of the central regions of these galaxies.

Sec. 2 is a description of the infrared photometry and a review of the optical photometry and spectroscopy. The data include resolved 2MASS photometry for 44 systems unresolved in the public catalogs and for 24 galaxies not detected or confused with nearby stars or galaxies. In Section 3 we investigate the infrared properties of the sample. We discuss the near infrared color-color diagram and investigate the relationships among the near and far infrared colors, the Balmer decrement, and the normalized star formation rate. In Section 4 we show that the star formation rate as indicated by the normalized far infrared flux increases as the projected pair separation decreases as expected if the interaction triggers star formation. There is also a suggestive increase in the spread of near infrared color as the projected separation of the pair decreases. This increased spread is evidence for triggered central bursts which may be either very blue or very heavily obscured and reddened. We conclude in section 5.

2. OBSERVATIONS AND DATA REDUCTION

2.1. The Sample of Pairs

BGK identified 358 close pairs and n-tuples in the original magnitude limited CfA2 redshift survey with $m_{zw} \leq 15.5$. The original CfA2North covers the declination range

$8.5^\circ < \delta_{B1950} < 44.5^\circ$ and right ascension range $8h < \alpha_{B1950} < 17h$ and includes 6500 galaxies (Geller & Huchra 1989; Huchra et al. 1990; Huchra, Geller & Corwin 1995). The original CfA2South covers the region $-2.5^\circ < \delta_{B1950} < 48^\circ$ and $20h < \alpha_{B1950} < 4h$ and includes 4283 galaxies (Giovanelli & Haynes 1985, 1989, 1993; Giovanelli et al. 1986; Haynes et al. 1988; Wegner, Haynes & Giovanelli 1993; Huchra et al. 1999; see also Falco et al. 1999 for updated data for CfA2 North and South).

The pairs were originally selected with line-of-sight velocity separations $\Delta V < 1000 \text{ km s}^{-1}$, projected separations $\Delta D < 50h^{-1} \text{ kpc}$, and $cz > 2300 \text{ km s}^{-1}$. In this pair sample, n-tuples result from pairs linked by common members as “friends-of-friends.” The 2300 km s^{-1} limit excludes the Virgo cluster and limits the angular sizes of the galaxies relative to the slit aperture we use for spectroscopy (Section 2.5). We use a Hubble constant $100 \text{ km s}^{-1} \text{ Mpc}^{-1}$ unless otherwise specified.

Ninety percent of the pairs have $\Delta V < 500 \text{ km s}^{-1}$, comparable with the typical pairwise velocity dispersion in the redshift survey (Marzke et al. 1995). We repeated all of the analysis below for pair samples restricted to $\Delta V < 500 \text{ km s}^{-1}$ (89% of the original sample) and $\Delta V < 400 \text{ km s}^{-1}$ (84% of the original sample); there are no significant differences in any results for any sample.

The pairs with $\Delta V > 500 \text{ km s}^{-1}$ appropriately lie within rich clusters where the local velocity dispersion exceeds the mean and the local density contrast substantially exceeds the mean; we include these pairs for completeness and for consistency with our previous analyses of this catalog. We use the BGK technique based on an estimate of the galaxy overdensity in a $5h^{-1} \text{ Mpc}$ sphere around each pair in the sample to compute the interloper fraction for the entire pairs sample, $\lesssim 20\%$. By restricting the pairs sample to regions of low density contrast, we also repeated our entire analysis for samples where the estimated interloper fraction is $\lesssim 10\%$. These restricted pair samples yield the same results we obtain for the full sample and provide reassurance that interlopers are not responsible for salient differences between the near infrared characteristics of pairs and the general galaxy population.

The pairs in the full sample we use were selected without explicit bias in morphology or environment. Updated coordinates and redshifts modify the sample slightly from the original one discussed in BGK; the sample we analyze here contains 791 rather than the 786 galaxies in BGK. These galaxies lie in 306 pairs, 37 triples, 8 quadruples, and 7 quintuples. From here on, for simplicity, we refer to all of the systems as pairs.

2.2. 2MASS photometry

2MASS is an all-sky survey with uniform, complete photometry (Nikolaev et al. 2000; Skrutskie et al. 2006) in three infrared bands J, H, and K_s . K_s is a modified version of the K filter designed specifically to reduce thermal background. For most of our analysis, we use the 20 mag arcsec $^{-2}$ isophotal elliptical aperture photometry from the final extended source catalog (XSC; Jarrett et al. 2000). We compare slit J,H,K magnitudes (Section 2.3) with the 2MASS 7" aperture magnitudes.

We downloaded JHK_s from the 2MASS extended source catalog using the IRSA web interface at IPAC¹. All 791 galaxies in the complete pairs sample are detected.

Among the BGK pairs, 44 systems (12%) are unresolved in 2MASS. The median recessional velocity, cz , of the BGK sample is only 5852 km s $^{-1}$. The unresolved pairs are a potentially serious problem for trying to use the 2MASS catalog for pair selection even at this depth and certainly as a basis for a deeper sample. One of us (T.H.J.) reanalyzed the 2MASS data to obtain magnitudes for the individual galaxies in the unresolved BGK pairs. For each galaxy, Table 1 lists the J2000 coordinate (column 1), the heliocentric radial velocity, cz (column 2), the J, H, and K_s 7" aperture magnitudes (columns 3, 4, 5 respectively) and the J, H, and K_s 20 mag arcsec $^{-2}$ isophotal elliptical magnitudes (columns 6, 7, 8, respectively). We indicate the previously unresolved objects with an asterisk in column 9. Twenty-four pair galaxies are either undetected or confused with nearby stars or nearby non-pair galaxies. T.H.J. also reanalyzed these pairs which are indicated by a + in column 9.

For 2MASS galaxies with $J \approx 11\text{--}13$, the photometric errors are $\sigma_J \approx 0.02\text{--}0.04$, $\sigma_H \approx 0.03\text{--}0.05$, and $\sigma_{K_s} \approx 0.04\text{--}0.06$ for the isophotal magnitudes, and $\sigma_J \approx 0.01\text{--}0.03$, $\sigma_H \approx 0.02\text{--}0.04$, and $\sigma_{K_s} \approx 0.03\text{--}0.05$ for the 7" aperture magnitudes. To estimate the uncertainty in the colors, we compute the average color differences

$$a_{J-H} = \langle |(J-H)_7 - (J-H)_{iso}| \rangle \quad (1)$$

and

$$a_{H-K} = \langle |(H-K)_7 - (H-K)_{iso}| \rangle \quad (2)$$

The subscript 7 refers to the 7" aperture colors and the subscript *iso* refers to the isophotal colors. For galaxies with $J \approx 11\text{--}13$, $a_{J-H} = 0.026$ and $a_{H-K} = 0.034$. Thus, the uncertainty in the typical 2MASS color is ~ 0.03 mag. This approach to the calculation of the error in the colors follows a procedure recommended by Press et al. (1992).

¹<http://irsa.ipac.caltech.edu/>

To compare the near infrared properties of the BGK sample with the general galaxy population, we use the Nearby Field Galaxy Sample (NFGS: Jansen et al. 2000a, 2000b). The NFGS was also selected from the Zwicky catalog, but the selection reproduces the galaxy luminosity function. Because it is drawn from a magnitude limited survey, the BGK sample is biased against the lowest luminosity galaxies sampled by the NFGS. We extracted 2MASS magnitudes for the NFGS galaxies and we compare the near infrared colors of the BGK pairs with the appropriate sample of representative NFGS galaxies. We restrict this comparison to the H-band luminosity range $\log(L_H) = 8.75 - 11.7$ L_\odot ($H_o = 73$ $\text{km s}^{-1} \text{ Mpc}^{-1}$) covered by both samples. There are 181 galaxies in the NFGS comparison sample.

2.3. Near Infrared Photometry

We acquired JHK images of 160 pair galaxies in the sample of BGK2 along with standard stars. These pairs are a random selection of the BGK pairs. We used several NIR cameras at the Fred L. Whipple Observatory 1.2-m and the Kitt Peak National Observatory (KPNO) 2.1-m telescopes. Table 2 summarizes pertinent details of the observing runs including the dates (column 1), the telescope (column 2), the imager (column 3) and the field of view (column 4). Each galaxy observation consists of five to nine 60 sec exposures, dithered by 30–75" in RA and Dec to allow for accurate sky-subtraction and the elimination of bad pixels during data reduction. All-sky observations of 10–14 Elias et al. (1988) and UKIRT photometric standards each clear night yielded accurate calibration constants and extinction corrections.

Our approach to reducing the IR camera data is based on previous experience with crowded Galactic fields with extended emission from reflection nebulae and H II regions (e.g. 5; 59; 22; 8; 4). Using a pipeline developed by W. Wyatt, we calibrated each frame with standard routines in NOAO IRAF². To generate flat-fields for each night, we median-filter all program frames using IMCOM, remove hot and dead pixels with a bad pixel mask, and normalize the median of the flat-field to unity. After dividing linearized program frames by the flat-field, we sort images by their median sky levels and select 11–15 images with sky levels closest to the median sky level of each program field. Median-filtered images of each set of 11–15 images, scaled by their median levels, yield sky frames for each program field. Sky-subtracted images with bad pixels removed have a median background level of zero and noise levels of 20.0–21.0 mag arcsec^{-2} at H.

²IRAF is distributed by the National Optical Astronomy Observatories, which is operated by the Association of Universities for Research in Astronomy, Inc., under contract to the National Science Foundation.

The technique to derive sky frames has several advantages over traditional methods. In ideal conditions where the sky background varies slowly and monotonically through the night, our approach yields sky frames composed of images acquired close in time to the program frame, as in standard reduction packages. When the sky background fluctuates erratically, our sky frames have fewer low level background features than traditional sky frames and do not require a DC offset to match background levels. Comparisons with traditional sky flats show that our approach reduces photometric errors by 0.01–0.02 mag.

To construct combined images for each pair, we use DRIZZLE (Fruchter & Hook 2002) in the STSDAS package within IRAF. Our procedure uses IMEXAM to derive (x,y) centers for each galaxy on each frame, DRIZZLE to shift the images to a common center, and IMCOM to construct a median-filter image of each galaxy from the set of DRIZZLED images.

We derive broadband magnitudes using a simple FORTRAN program to sum the flux in a rectangular aperture which replicates the size and orientation of the slit used for spectroscopic observations (Section 2.5). The program uses the (x,y) coordinates of the peak intensity to center the slit on each galaxy. Tests indicate uncertainties of 0.01–0.02 mag for ± 1 pixel (0.3–1.2 arcsec) uncertainties in the slit position and ± 1 pixel uncertainties in the size of the slit.

We estimate photometric uncertainties for the survey from repeat measurements. The uncertainty in the photometric calibration for each night is 0.01–0.03 mag. Multiple measurements of each galaxy within an observing run yield a typical uncertainty of ± 0.03 mag for galaxies with $H = 13\text{--}15$. Repeat measurements acquired on different observing runs indicate a similar uncertainty. The median offset between different observing runs is ± 0.02 mag. We thus conclude that the typical photometric uncertainty in our slit magnitudes is ~ 0.04 mag.

To estimate the uncertainty in the colors from our slit magnitudes, we derive colors assuming a fixed slit position for all three bands. Repeat measurements of galaxies throughout a single observing run and between observing runs yield identical color uncertainties of ± 0.04 mag in the J-H and H-K colors. This error estimate is smaller than the ± 0.06 mag uncertainty expected from simply adding the errors of individual bands in quadrature. However, we determine the color at a fixed slit position for all three bands. Thus the error in the slit position should not be included in the error in color. We therefore reduce the error in the color by removing the uncertainty in slit position relative to the spectroscopic aperture, $\sqrt{2(0.02)^2} \approx 0.03$ mag, and by the median offset in the photometric calibration between observing runs, ~ 0.02 mag, which yields an expected error, ≈ 0.04 mag, that agrees with the measured uncertainty.

Table 3 lists the measurements. Column (1) is the J2000 galaxy coordinate, column (2) is the slit length, L , in arcseconds, column (3) is the slit width, w , in arcseconds, column (4) is the slit position angle in degrees, and columns (4)-(6) are the corresponding J, H, and K slit magnitudes respectively. For nine galaxies without optical spectra (marked with an asterisk in column 7 of Table 3), we adopted the median slit length, $20''$, and the typical position angle of 90° . The colors of these galaxies span the range of J-H and H-K colors of other galaxies in the sample.

Fig. 1 compares the colors derived from our slit magnitude with 2MASS colors derived from the 2MASS $7''$ diameter magnitudes. We use the 2MASS small aperture magnitudes here because they are the best available match to our slit magnitudes. The smaller points indicate galaxies with 2MASS isophotal $J > 13$. The mean color difference $\langle (J - H) - (J - H)_{2M} \rangle = -0.03 \pm 0.005$; $\langle (H - K) - (H - K_s)_{2M} \rangle = 0.01 \pm 0.005$. Removing the large outliers in Fig. 1, the dispersion in $\sigma[(J - H) - (J - H)_{2M}] = 0.05$ mag; and $\sigma[(H - K) - (H - K_s)_{2M}] = 0.05$ mag. The typical errors in the 2MASS colors are 0.03 mag: $\sigma[(J - H) - (J - H)_{2M}]$ and $\sigma[(H - K) - (H - K_s)_{2M}]$ are thus consistent with the 0.04 mag error we estimate in our slit aperture photometry. These measures refer to the ensemble of points in the plots. We suspect that the small blueward offset of our J-H relative to 2MASS results from differences in the aperture; our extracted apertures tend to be somewhat larger than 2MASS $7''$ aperture. The reddest outliers in $(H - K) - (H - K_s)_{2M}$ occur because our broader K filter provides greater sensitivity to emission from hot dust³ (see Hunt et al. 2002 and Sections 3.1 and 3.2 below).

2.4. IRAS data

We downloaded 12–100 μm photometry from the IRAS extended and point source catalogs using the IRSA web interface (Beichman et al. 1985). These data yield 246 matches to pair galaxies, with 156 systems having both reliable 2MASS and 60 μm photometry. All but 10 of these 156 systems have reliable 100 μm fluxes. In 5 pairs, IRAS unambiguously detected both galaxies; in 47 pairs, IRAS detected one of the galaxies unambiguously; in 107 pairs, the IRAS detection is unresolved.

Table 4 lists sample IRAS data for ten BGK pairs of galaxies. We include a J2000 BGK coordinate designation (column 1), IRAS B1950 coordinate designation (column 2),

³With a full-width at half maximum of 0.4 μm (2–2.4 μm), the standard K filter is 25% wider than the K_s filter, which has a full-width at half maximum of 0.3 μm (2–2.3 μm). We acquired our K data in dry conditions, where K is more sensitive than K_s to hot dust emission with $T = 600\text{--}1000$ K.

and the IRAS photometry (columns 3-6). The typical error in the $60\ \mu\text{m}$ detections is 0.25 Jy; in the $100\ \mu\text{m}$ detections it is 0.5 Jy. The typical error in the upper limits at $60\ \mu\text{m}$ is 0.5 Jy. In this Table, we associate the IRAS flux with the pair galaxy closest to the IRAS coordinate. In our discussion we treat the IRAS emission as a property of system; the poor spatial resolution of IRAS prevents robust association with individual galaxies.

The sample of pairs resolved by IRAS (SSM) offers some insight into the completeness of the IRAS identifications we make in the BGK sample. The BGK sample contains all pairs in a magnitude limited redshift survey with projected separations $< 50h^{-1}$ kpc; the SSM pairs are restricted to systems separated by fewer than 3 galaxy diameters. Interestingly, the BGK sample contains 4 pairs within the 5.24 Jy limit of the SSM sample, but they are too widely separated to meet the SSM diameter criterion. Table 5 lists these pairs: column (1) gives the J2000 coordinate of the BGK galaxy closest to the IRAS source, column (2) gives the IRAS B1950 identification, and columns (3-6) give the IRAS fluxes.

In most of the SSM pairs, the galaxies are too faint at B to be included in BGK. However 33 of the SSM pairs lie within the limits defined by the selection of the BGK sample. Among these, two pairs are missing from the BGK sample because the galaxies were not resolved in the original Zwicky et al. (1961-1968) catalog on which the redshift survey was based. Unresolved pairs at small angular separation are a limiting factor for all samples of close pairs. All told, the BGK and SSM samples have 31 pairs in common and differ by a total of 6 pairs in the range of complete overlap.

As we did for the BGK pairs, we also extracted 2MASS magnitudes for the SSM pairs. We use these data only to show that the SSM pairs include more extreme dusty objects than the BGK sample. The Appendix compares further basic IRAS properties of the BGK and SSM pairs. More detailed comparison of these pair samples is beyond the scope of this paper because of the complex selection of the SSM pairs and because we do not have spectroscopy for them.

2.5. Spectroscopy

BGK and BGK2 describe the spectroscopic observations and data reduction in detail. Here we briefly review the procedures we used.

We made observations of 502 galaxies with the FAST spectrograph at the 1.5 meter Tillinghast telescope on Mt. Hopkins. We observed each galaxy for $\sim 10\text{-}20$ minutes through a $3''$ -wide slit and used a 300 line/mm grating to disperse the light over $4000\text{-}7000\text{\AA}$.

Our spectra are representative of the “central” region of each galaxy. The apertures extracted from the flat-fielded data range in length from 1.74 to 29.7” corresponding to 0.25 - 13.7 h^{-1} kpc with a mean of 2.4 h^{-1} kpc (see Table 4). The measured equivalent widths are the ratio of the flux in the line to the surrounding continuum corrected for Balmer absorption. We estimate the amount of absorption by taking the maximum absorption equivalent width in $H\delta$ or $H\gamma$, and then adding that equivalent width to both $H\alpha$ and $H\beta$. Table 1 of BGK2 lists the $EW(H\alpha)$ and $H\alpha/H\beta$ for the galaxies in our sample. The typical error in the $EW(H\alpha)$ is 10%; in the Balmer decrement, the error is typically 20%. Repeat measurements suggest that the error results largely from uncertainty in the slit position.

We remove active galactic nuclei (AGNs) and “ambiguous” objects which may be AGN dominated from both the BGK and NFGS samples by using the theoretical optical classification scheme developed by Kewley et al. (2001). There are 3 such objects in the NFGS (Kewley et al. 2002); there are 32 objects in BGK spectroscopic sample. Because the number of these objects is small, removal has a negligible effect on the analyses below; we remove the objects for consistency in our focus on star formation. Among the 265 galaxies without spectra, we expect about 17 AGN and/or “ambiguous” galaxies, a residual number too small to impact any trends in the dataset. In any case, the mean J-H of the BGK AGN and “ambiguous” galaxies is 0.02 mag bluer and their H-K is 0.02 mag redder than the 470 non-AGN galaxies in the spectroscopic sample.

3. The Near Infrared Properties of Galaxy Pairs

Although the near infrared colors of galaxies span a narrow range, they provide an interesting window on star-forming galaxies. In this section we explore the infrared properties of the BGK sample. Even though the BGK sample is B-selected, the sample is nearby enough that the pairs can be resolved in 2MASS and *all* of the galaxies are detected in 2MASS.

The near-infrared probes a complex combination of stellar population, reddening, and gaseous and thermal dust emission. We use our own infrared photometry and spectroscopy to probe these issues. For this exploration our photometry has two advantages over 2MASS: (1) we extract photometry in the aperture where we have spectroscopy and (2) we use the standard K filter which extends to longer wavelength than the 2MASS K_s . The K filter is more sensitive to thermal emission from 600 — 1000K dust.

3.1. The Near Infrared Color-Color Diagram

The near infrared colors for a normal unreddened stellar population span a small range in J-H and H-K_s (Aaronson 1977, Giuricin et al. 1993). By collecting data from two sets of close pairs selected either by optical morphology or by projected separation and line-of-sight relative velocity, Giuricin et al. concluded that “interacting” galaxies display normal J-H colors and redder H-K colors than a “normal” galaxy population. Making use of the existing L-band data, they also concluded that the redder H-K colors indicate the presence of thermal emission from hot 600 — 1000K dust. Here we compare the J-H and H-K colors for the BGK sample of close pairs with the NFGS sample of “normal” galaxies and with the SSM sample of IRAS-selected pairs.

We have assembled data for a much larger sets of both pairs and normal galaxies than considered by Giuricin et al. (1993) and Aaronson (1977), respectively. The errors in the infrared colors for galaxies in the Giuricin et al. (1993) sample are typically 0.1 in J-H and 0.06 in H-K, substantially exceeding the errors in our data. The sample considered by Giuricin et al. (1993) is an exhaustive compilation of inhomogeneous infrared data from the literature, but the sample is not complete in any band. The pair sample we consider is a complete B limited sample with near infrared photometry for all objects. We examine the sample in the broader context of a similarly selected sample of “normal” galaxies from the NFGS and the far infrared selected sample of SSM. In all cases the near infrared data are uniformly acquired from 2MASS.

The panels of Fig. 2 show color-color diagrams for the 2MASS JHK_s data (upper left) and for our JHK data (upper right) for the individual galaxies in the BGK pairs. To set the BGK sample in a broader context, we also show 2MASS data for the individual galaxies in the SSM pairs (lower left) and for the NFGS sample of “normal” galaxies. K-corrections for galaxies in these samples are small, typically $\lesssim 0.03$ at K_s and $\lesssim 0.01$ at J and H (Poggianti 1997). In the NFGS panel (lower right), the curves show how the colors of solar neighborhood stars on the main sequence (solid curve) and giant branch (dot-dashed curve) bracket the “normal” galaxy colors (Bessell & Brett 1988).

In all of the panels of Fig. 2 the line with ticks shows the contribution at K from thermal emission by dust with a temperature of 1000K; each tick marks a 10% increase in the hot dust contribution. The arrow indicates the reddening vector (Bessell & Brett 1988).

The NFGS sample of “normal” optically selected galaxies spans the expected narrow range of near infrared colors. K-S tests show that the probability that the J-H and H-K_s distributions for the BGK and NFGS samples are drawn from the same parent distributions are 1.6×10^{-12} and 8.5×10^{-10} , respectively. Both the mean J-H and H-K are slightly redder

in the BGK sample than in the NFGS and the spread in both colors is larger, consistent with the results of Cutri and McAlary (1985). Giuricin et al. (1993) were unable to see the difference in the distribution of J-H for pairs in their smaller sample.

In our sample of pair galaxies the scatter in near infrared colors is both toward red J-H and H-K and toward blue J-H and H-K than the NFGS. As we discuss below this behavior results from the presence of young central bursts of star formation which scatter the colors blueward and from dusty bursts which scatter the colors redward. The original selection of the sample at B and subsequent "observation" in the near infrared favors detection of the blueward scatter relative to the detection of dusty bursts. Selection in a redder band favors the redward scatter relative to the blueward scatter introduced by relatively unobscured bursts; we demonstrate this point by examining the SSM IRAS-selected pairs.

As expected, the SSM sample, selected at $60\mu\text{m}$, shows a notable extension toward red H- K_s , much more impressive than in our B-selected dataset. Because we do not have complete spectroscopy for this sample, we cannot remove the AGNs; however, it is improbable that all of the reddest objects in H- K_s are AGN. There are 16 known AGNs in the SSM sample (Veilleux et al. 1995; Kewley et al. 2001; Corbett et al. 2003). These AGN have mean near infrared colors $J-H = 0.74 \pm 0.02$ and $H-K_s = 0.33 \pm 0.01$ consistent with the overall mean for the sample. Only one of these AGN is a red outlier in H- K_s . Based on the properties of the known AGN, we expect only 2-4 red outliers in H- K_s even if 30% of the SSM galaxies are AGN. The well-populated extension toward red H- K_s is thus very probably a property of star-forming objects.

Without longer wavelength data, particularly at L, there is also an ambiguity in the relative contributions of reddening and dust emission for star-forming objects with $0.4 < H-K_s < 0.5$. However, even in the narrow K_s filter, it is essentially impossible to explain the full extension of the colors of star-forming galaxies in the SSM sample along the dust emission track in Fig. 2 by any other straightforward mechanism (Hunt et al. 2002).

In our B selected pairs sample, the bluest galaxies are generally faint in the near infrared; these objects also tend to have the lowest intrinsic B-band luminosities in the pairs sample. Many of these objects have $J > 13$ and thus appear as small points in the color-color diagram. They tend to appear at blue J-H with a range of H- K_s . It is interesting that the SSM sample which includes nearby intrinsically low luminosity objects also includes pair galaxies with these bluer J-H colors. Overall, the larger range of near infrared colors of pairs compared with the NFGS is independent of the inclusion of these fainter objects although they accentuate the difference in the expected sense. Appendix A contains a more extensive comparison of the properties of the SSM and BGK samples.

The upper right hand panel of Fig 2 shows our JHK slit aperture photometry for a subset of 160 BGK galaxies. More objects in this subset extend toward redder J-H and H-K than in the 2MASS BGK color-color diagram (upper left panel). There are two reasons for this extension. Although color gradients are generally small in the infrared, some objects are significantly redder in their central regions (Griersmith et al. 1982; Glass & Moorwood 1985; Devereux 1989; Bushouse & Werner 1990; Carico et al. 1990; Jarrett 2000; Kewley et al. 2005). The broader K filter is also more sensitive to hot dust emission which has a negligible effect on J-H but produces a redder H-K. We discuss these JHK colors in more detail below.

To understand the difference between the color-color diagrams for the BGK pair sample and NFGS sample of normal galaxies, we construct a simple model. The model is intended to account qualitatively for the spread of colors rather than to explain details of individual cases. The model has six ingredients: (i) an estimate of the mean color for a “normal” galaxy population, (ii) the spread in color which represents both the intrinsic spread of a “normal” population and the measurement error, (iii) reddening, (iv) emission from a young stellar population associated with a burst of star formation, (v) gaseous emission from HII regions, and (vi) thermal reradiation from hot dust. The schematic in Fig. 3 shows the normal range of near infrared colors (error bar) along with arrows indicating the direction of the effect of the various contributors to the near infrared colors.

To reconstruct the distribution of colors for galaxies in the BGK sample, we begin with the median colors of the NFGS: $(J-H)_o = 0.67$ and $(H-K_s)_o = 0.27$. The mean E_{B-V} for the NFGS in our luminosity range is 0.28 ± 0.03 . The median NFGS colors are completely consistent with earlier studies (see e.g. Aaronson 1977; Giuricin et al. 1993).

To account for the spread of colors in a “normal” galaxy population and for the measurement error in the colors, we first add a dispersion of 0.05 mag in both colors, denoted by σ_{J-H} and σ_{H-K} in Table 6. With a typical 2MASS color error of 0.03 mag, the intrinsic dispersion in color we assume is 0.04 mag, consistent with the results of Aaronson (1977). We select a random additional reddening by taking the absolute value of a Gaussian with a dispersion of 0.020 in the extinction at $H-K_s$, E_{H-K_s} . We denote this contribution by σ_R in Table 6. The extinction at J-H, $E_{J-H} = 1.95 E_{H-K_s}$. The dispersion σ_R corresponds to an *additional* $A_V = 0.3$ (Bessell & Brett 1988) and moves the colors redward along the reddening vector. Fig. 3 (model R: upper right panel) shows that this simple prescription accounts for most of the range and for the redward shift in the color-color diagram for the BGK pairs, but outliers remain particularly toward the bluest J-H and reddest H-K_s.

We can account statistically for most of the outliers by including contributions from young stellar populations, free-free emission and dust. Models B and G explore the effect

of adding a burst of star formation and gaseous emission respectively. Table 6 gives the parameters for these models; column (1) gives the model designation, columns (2) and (3) list the fiducial colors, $(J-H)_0$ and $(H-K)_0$, columns (4) and (5) give the “normal” spread of $J-H$ and $H-K$ colors, respectively, columns (6-9) give the contributions from a young burst, hot dust, gaseous emission, and reddening, respectively. The models are not unique; they are intended to demonstrate the impact of the various contributions to the near infrared emission and to show that reasonable parameters account for the observed spread of colors.

Model B in the lower left panel of Fig. 3 shows model R with the addition of a burst contribution. In this example the burst color is $J-H = H-K_s = 0$, characteristic of A stars. For this demonstration, we ignore the complexities of variation in the initial mass function, metallicity, and spread in age and duration of the bursts. We select the fractional contribution of the “burst” at H by taking the absolute value of a Gaussian with a dispersion of 0.05; we denote this contribution by σ_B in Table 6. This choice is consistent with BGK2s optical analysis of burst strengths. For the 40-60% burst strengths most common in the BGK2 sample, a 5% burst contribution at H corresponds to a roughly 50% contribution at R for the typical $R-H \sim 2.5$ we measure in the slit aperture for the bluer objects. Addition of a “burst” moves the colors blueward in both $J-H$ and $H-K_s$.

Model G in the lower right panel of Fig. 3 shows model R with the addition of gaseous emission with a color of $J-H = 0$ and $H-K_s = 0.7$ (Campbell & Terlevich 1984; Whitelock 1985; Larios & Phillips 2005) The addition of gaseous emission moves the colors blueward in $J-H$ and redward in $H-K_s$. We select the fractional contribution of the gaseous emission at H by taking the absolute value of a Gaussian with a dispersion of 0.08 and denote this contribution by σ_G in Table 6.

Fig. 3 shows that our heuristic model accounts for the colors of all but a few extreme outliers. The outliers with blue $H-K_s$ and red $J-H$ are fainter than $J = 13$ and may have large errors in their colors. The two very blue objects in $J-H$ may be dominated by a strong burst and/or gaseous emission. The reddest object in both $J-H$ and $H-K_s$ requires at least a 10% contribution from hot dust emission at K_s .

For the BGK sample, our small aperture broader K band data underscore the necessity of accounting for emission from hot dust in modeling the interaction. These conclusions are in accord with Giuricin et al. (1993). In the model shown in Fig. 4, $(J-H)_0 = 0.72$; $(H-K)_0 = 0.20$, the error in $J-H$ and $H-K$ is 0.06 mag, corresponding to a color error of 0.04 mag and an intrinsic spread in color of 0.045 mag. We draw the additional reddening from a Gaussian with a dispersion of 0.06 in $H-K$, the fractional contribution from gaseous emission at H is drawn from a Gaussian with a dispersion of 0.04, the fractional “burst” contribution at H is drawn from a Gaussian with a dispersion of 0.08. To match the extension toward the

reddest H-K, we introduce a contribution from dust emission. The fractional dust emission contribution at H is drawn from a Gaussian with a dispersion of 0.008 and denoted by σ_D in Table 6. At K, this dispersion is 0.09. Thus the dust contribution for the reddest objects in H-K is 10-20% at K.

Fig. 5 shows images of a few of the objects in our infrared small aperture photometry sample with the reddest central H-K colors. For the red objects in the left and central panels, there is no spectroscopic evidence of AGN activity. We exclude the AGN in the righthand panel from the sample; its blue companion has an $\text{EW}(\text{H}\alpha) = 37\text{\AA}$.

The Infrared Space Observatory (ISO) provided the first suggestion of hot 600-1000 K dust in star-forming galaxies (Helou et al. 2000). Subsequent JHK L' observations demonstrate that some actively star-forming galaxies have $K-L' \geq 1$, consistent with hot dust emission (Hunt et al. 2002). Hunt et al. (2002) suggest that the hot dust is associated with the intense far ultraviolet radiation field in compact (≤ 100 pc) regions of active star formation which might arise naturally from galaxy-galaxy interactions and mergers. In their sample of 26 galaxies, they were unable to detect any correlation between the presence of hot dust and the much cooler dust.

For the BGK pairs the ratio of 60 μm to 100 μm IRAS fluxes implies emission from dust at temperatures in the range 20-70K assuming a blackbody spectrum (Beichmann et al. 1985). We do not have enough pairs with both small aperture photometry and IRAS detections to make a meaningful comparison of H-K with L_{FIR}/L_H ; we thus use the much larger sample of 2MASS H-K_s data to see whether there is any relationship between the presence of hot dust and far infrared emission from cooler dust.

Fig. 6 shows the distribution of the normalized far-infrared luminosity L_{FIR}/L_H as a function of H-K_s for the BGK pairs. We define the far infrared flux in the standard way (Helou et al. 1988; Sanders & Mirabel 1996):

$$F_{\text{FIR}} = 1.26 \times 10^{-14} \{2.58f_{60} + f_{100}\} \text{Wm}^{-2}$$

where f_{60} and f_{100} are the 60 μm and 100 μm fluxes respectively. If a pair is resolved we sum the fluxes for the components; for each pair the luminosity we plot represents the total for the pair and the H-K_s color is the appropriately weighted “pair” color.

Fig. 6 shows L_{FIR}/L_H as a function of H-K_s from 2MASS for the BGK pairs for both IRAS detections and upper limits. L_{FIR} is proportional to the star formation rate (Kennicutt 1988; Calzetti et al. 2000; Charlot et al. 2002; Kewley et al. 2002) and L_H is a measure of the stellar mass. Thus L_{FIR}/L_H provides a measure of the normalized or specific star formation rate. Fig. 6 shows that the reddest H-K_s colors correspond to relatively large

F_{FIR}/F_H . Using the ASURV package (Lavalley et al. 1992), the Spearman rank probability of no correlation including the upper limits in Fig. 6 is $< 10^{-4}$. The increasing scatter in $H-K_s$ with increasing F_{FIR}/F_H is also a striking feature of Fig. 6. At the bluest $H-K_s$, all of the points with large F_{FIR}/F_H are upper limits (open triangles); nearly all of the reddest $H-K_s$ are detections at large F_{FIR}/F_H . The data suggest that the reddest galaxies in $H-K_s$ contain dust emitting over a wide temperature range. These data indicate that, as suggested by Hunt et al. (2002), some galaxies which undergo strong central bursts of star formation and thus have substantial specific star formation rates contain compact star-forming complexes with very red $H-K_s$. These regions may be similar to the dusty super-star clusters found in interacting galaxies and ULIRGs (e.g. Gallagher & Smith 1999; Bekki & Couch 2001; Keel & Borne 2003; Kassin et al. 2003)

Emission from hot dust may also be associated with AGN activity. We have removed the spectroscopically identifiable AGN from our sample. However, we show in the next section that the reddest objects in $H-K$ have weak or even undetectable $H\alpha$ emission. It is possible that AGN activity is hidden. Because AGNs are rare in the large sample we can classify spectroscopically, we favor vigorous star formation as the explanation of the reddest $H-K$ colors. Hard x-ray observations with *Chandra* and mid infrared imaging with *Spitzer* would be useful in better identifying AGNs (Alonso-Herrero et al. 2006).

It is frustrating that in Fig. 6, the poor resolution of IRAS prevents plotting quantities for individual galaxies that can be readily identified with points in the color-color diagrams. Clearer tests of the underlying physics which dominates the color-color plots requires the resolution of *Spitzer*. Hopefully large objectively selected samples of nearby pairs with *Spitzer* observations will soon be forthcoming.

3.2. Spectroscopy and Infrared Colors

We next use our spectroscopy to elucidate further the physics which underlies the color-color diagrams. We combine the spectroscopy with our JHK photometry in the spectroscopic aperture. Fig. 7 shows the relationship between the Balmer decrement and the $J-H$ color (see Moorwood et al. (1987) for the first demonstration of this particular correlation but without a fitted slope). With the exception of a few outliers, it is remarkable that these objects, some of which contain young or heavily reddened bursts of star formation, have essentially the same reddening law as the Galaxy. The Spearman rank probability of no correlation is 10^{-4} and the best fit slope (16.2 ± 1.9 , $\chi^2/\text{dof} = 2.1$; dot-dashed line) is close to the Galactic reddening law (14.0; solid line; Bessel & Brett 1988).

A large $\text{EW}(\text{H}\alpha)$ indicates a strong burst of star formation. BGK2 conclude that these bursts can account for 40-60% of the galaxy light at R. These substantial bursts should result in bluer than normal near infrared colors. Fig. 8 shows the J-H color as a function of the $\text{EW}(\text{H}\alpha)$. Indeed at the very bluest colors ($\text{J-H} \lesssim 0.57$), 55% of the galaxies have $\text{EW}(\text{H}\alpha) \gtrsim 25 \text{ \AA}$ and 9% have $\text{EW}(\text{H}\alpha) \lesssim 10 \text{ \AA}$. At $\text{J-H} \gtrsim 0.78$, 11% of the galaxies have $\text{EW}(\text{H}\alpha) \gtrsim 25 \text{ \AA}$ and 56% have $\text{EW}(\text{H}\alpha) \lesssim 10 \text{ \AA}$. The Spearman rank probability of no correlation is 6.8×10^{-5} . The $\text{EW}(\text{H}\alpha) = 0$ objects have a major impact on the Spearman rank probability; eliminating them gives a probability of 0.11 of no correlation.

Fig. 7 shows that the Balmer decrement is less well correlated with H-K; the Spearman rank probability of no correlation is 0.26. We see little correlation here because dust emission affects H-K but not J-H (see the schematic in Fig. 2 and the model in Fig. 3 which requires dust emission to account for the data). The dot-dashed line indicates the best fit slope 5.8 ± 0.4 , with an abysmal $\chi^2/\text{dof} = 41$. The solid line shows the slope of the standard Galactic reddening law (21.4; Bessell & Brett 1988).

Fig. 9 shows the relationship between $\text{EW}(\text{H}\alpha)$ and H-K. The apparent correlation is not significant; the Spearman rank probability of no correlation is 0.65. The largest $\text{EW}(\text{H}\alpha)$ occur at bluer $\text{H-K} \lesssim 0.35$; 10% of galaxies with $\text{H-K} \lesssim 0.35$ have $\text{EW}(\text{H}\alpha) \gtrsim 50 \text{ \AA}$. None of the reddest galaxies ($\text{H-K} \gtrsim 0.45$) have $\text{EW}(\text{H}\alpha) \gtrsim 50 \text{ \AA}$. Although most of the reddest galaxies have $\text{EW}(\text{H}\alpha) \lesssim 10 \text{ \AA}$, there are also objects at blue H-K with $\text{EW}(\text{H}\alpha) = 0$.

In Figs. 8 and 9, boxed symbols indicate galaxies with non-zero $\text{EW}(\text{H}\alpha)$ but without a measurable $\text{F}(\text{H}\alpha)/\text{F}(\text{H}\beta)$. Of the five objects with $\text{H-K} > 0.5$ (these objects are the most likely to contain dusty compact regions of intense star formation) two have $\text{EW}(\text{H}\alpha) = 0$, two have immeasurable Balmer decrements, and one has $\text{F}(\text{H}\alpha)/\text{F}(\text{H}\beta) \sim 5$. All of these objects are in IRAS-detected systems with $\text{L}_{\text{FIR}}/\text{L}_H \gtrsim 1.8$. The member galaxies thus may contain dust enshrouded bursts. Accounting for these “hidden” bursts is important for a full picture of tidally triggered star formation and for calculations of the star formation rate density throughout the universe.

4. The Infrared and Triggered Star Formation

In this section we investigate the relationship between the infrared properties of the BGK pairs and the projected separation of the pair, a measure of the interaction. An impressive range of star-formation indicators are correlated with the projected separation including the $\text{EW}(\text{H}\alpha)$ (BGK, BGK2), the star formation birth rate parameter for pairs in the 2dF survey (Lambas et al. 2003; Alonso et al. 2004), the mean specific star formation

rate derived from Sloan Digital Sky Survey (SDSS) $\text{H}\alpha$ and z-band luminosities (Nikolic et al. 2004), the concentration index measured in the r-band as a measure of the presence of nuclear bursts of star formation (Nikolic et al. 2004), and metallicity as an indicator of gas infall in the BGK pairs (Kewley et al. 2006).

4.1. Far Infrared Specific Star Formation Rates

Fig. 10 shows the normalized distribution of projected separations for pairs in the BGK sample with and without IRAS detections. The KS probability that the two distributions are drawn from the same population is 3.3×10^{-4} . The pairs detected in IRAS have a median separation of $20 \text{ } h^{-1} \text{ kpc}$; the median for the undetected pairs is $32 \text{ } h^{-1} \text{ kpc}$. These distributions suggest that pairs which are most probably close together in space have greater specific star formation rates.

To explore the connection between specific star formation rate and ΔD further, we calculate $\log(F_{FIR}/F_H)$ (solid dots) or the upper limit on $\log(F_{FIR}/F_H)$ (open triangles) for each BGK pair. Fig. 11 shows the distribution of $\log(F_{FIR}/F_H)$, a proxy for the specific star formation rate, as a function of ΔD , for pairs with $\Delta D < 60 \text{ } h^{-1} \text{ kpc}$.

To examine the correlation between specific star formation rate and ΔD we use the ASURV package (Lavalley et al. 1992) which treats the upper limits. The Spearman rank probability of no correlation is $< 10^{-4}$. Smaller ΔD favors larger $\log(F_{FIR}/F_H)$.

For comparison with Fig. 11, Fig. 12 shows the $\text{EW}(\text{H}\alpha)$ as a function of ΔD for the entire BGK sample. In contrast with Fig. 11 where the IRAS resolution limits us to plotting fluxes for systems, we plot $\text{EW}(\text{H}\alpha)$ for individual galaxies in Fig. 12.

Nikolic et al. (2004) discuss the normalized FIR star formation rate as a function of separation for a subset of their SDSS pairs. They consider only IRAS detections and discuss the inherent bias in that approach. They conclude that the normalized star formation rates calculated from $\text{H}\alpha$ emission or from FIR fluxes decrease with increasing projected separation in agreement with our conclusion derived from both detections and upper limits. A serious limitation on comparison of the spectroscopic and FIR indicators of the star formation rate is that our spectroscopic measurements are limited to a central aperture; the IRAS fluxes rarely even resolve the pair.

BGK and BGK2 plot the relation in Fig. 12 for subsets selected by local density. Like Nikolic et al. (2004) and other investigators, we make no density selection here. The Spearman rank probability that the data are uncorrelated is $< 10^{-4}$, consistent with the

result based on the IRAS fluxes and upper limits for the same sample.

The data provide strong evidence for a relationship between the normalized star formation rate and the projected separation of the pair regardless of the measure we use for the star formation rate. It would be fascinating to see a similar plot for galaxies in pairs with complete spectroscopy observed with *Spitzer* so that a more direct comparison could be made between the star formation rate indicators for a large objectively selected pair sample.

4.2. Near Infrared Colors

The situation in the near infrared is complex. Dust emission produces a redder H - K_s but leaves J-H essentially unchanged. Reddening produces generally redder near infrared colors and a burst of star formation produces bluer colors. Gaseous emission produces bluer J-H and redder H-K. Because of the multiplicity of sources of near infrared emission and because the full range of near infrared colors of stellar populations is small, the near infrared colors alone are not useful for estimating the strength of a burst of star formation.

The near infrared color-color diagram (Fig. 2) shows that the distribution of near infrared colors of close pairs differs from a sample of “normal” galaxies. For a more complete model, L-band and resolved 60 μm photometry are necessary to separate the effects of reddening from the effects of dust emission. Nonetheless, the near infrared colors indicate a possibly interesting dependence on the projected separation of the pair.

Fig. 13 shows the near infrared color color diagrams for the slit aperture JHK sample divided at the median separation, $\Delta D = 21h^{-1}$ kpc. There are 80 galaxies in each of the two subsamples. The two subsamples appear different to the eye in the sense that the spread in colors, particularly H-K, is larger at smaller separation; all of the bluest and reddest objects at H-K are at smaller projected separations. There are outliers in H-K toward the blue (indicating central bursts of star formation) and toward the red (indicating dusty bursts). It is interesting that the outliers in the small ΔD sample are in the directions indicated in the schematic of Fig. 3 for young burst and dust emission contributions. All of the candidate dust enshrouded bursts with H-K > 0.5 are in pairs with small projected separation. However, a 2D KS test shows the samples have a 10% probability of being drawn from the same underlying distribution.

Fig. 13 suggests that the range of colors may be greater for tighter pairs, but the strength of the conclusion may be limited by the sample size. The 2MASS data also yield insignificant differences in color distribution with projected separation, but the 2MASS aperture is large and the 2MASS K_s is less sensitive to the effects of dust. Exploration of a larger sample of

small aperture data would be worthwhile especially with the addition of L-band data. There is potential for detecting both the impact of dusty bursts and blue bulges in this approach.

5. Conclusion

We use the BGK sample of pairs of galaxies selected from the complete CfA2 redshift survey to examine near and far infrared photometry for clues to the nature of the galaxy-galaxy interaction. The depth of the CfA2 survey is well-matched to 2MASS and all of the nearly 800 galaxies in the sample have 2MASS photometry. The sample of close pairs we analyze is much larger than those considered in previous investigations of the infrared properties of close pairs.

We use a combination of 2MASS photometry, deep JHK photometry in small apertures, spectroscopy, and IRAS data to explore the infrared as a probe of triggered bursts of star formation. We find:

1. The distribution of J-H, H-K_s, and H-K colors of pairs is broader than the corresponding distribution for a sample of “normal” galaxies. We interpret this difference as evidence for bursts of star formation which produce an extension toward bluer colors and for a combination of reddened and/or dusty bursts which produce an extension toward redder colors, particularly in H-K. In the color-color diagram the reddest objects in H-K are also red in J-H. The colors of these objects follow a track for thermal emission from 600-1000K dust. The reddest H-K colors require emission from hot dust.
2. A statistical model including emission from a young stellar population, gaseous emission from HII regions, and emission from hot dust explains the outliers in infrared color-color diagrams. This model shows that triggered central bursts affect the near infrared colors. The effects are complex because of the multiplicity of emission processes important in the near infrared.
3. We use our spectroscopy and small aperture photometry to show that the central J-H colors and Balmer decrements are consistent with the Galactic reddening law. However H-K colors are essentially uncorrelated with the Balmer decrement as a result of emission from hot dust.
4. We identify a set of objects with central H-K ≥ 0.45 , with $F_{FIR}/F_H \gtrsim 1.8$, and with small EW(H α). We argue that these objects harbor compact dust enshrouded bursts possibly similar to the super-star clusters identified in well-studied interacting galaxies. These objects may be examples of “hidden” bursts or, possibly, “hidden” AGN. Their

presence supports the contention that H α surveys underestimate the volume averaged star formation rate in the nearby universe.

5. We examine measures of the specific star formation rate as a function of the projected separation of the pairs in our sample. Both spectroscopic and far infrared photometric measures show that the specific star formation rate decreases with increasing projected separation. The poor spatial resolution of IRAS prevents direct comparison of these measures.
6. Examination of the near infrared color-color diagram as a function of projected separation shows that all of the outliers indicative of a central burst of star formation lie in pairs at small separation. Although our sample is too small to make the case for a statistically significant dependence of the near infrared color-color diagram on projected separation, the data suggest that larger samples of deep, small aperture near infrared photometry would be a basis for identifying both the very blue and very red central bursts. An increase in the dispersion might be expected as a result of triggered bursts which produce blue central regions in the absence of dust and very red central regions in the presence of dust.

Taken together these results indicate that a larger sample of pairs with complete spectroscopy and with small aperture near infrared photometry and resolved mid-infrared photometry from *Spitzer* would be an important dataset for isolating the effects of young bursts, reddening, and thermal dust emission over the course of galaxy-galaxy interactions and subsequent mergers.

We thank Jason Surace for providing early versions of the computer readable tables from SSM. We thank the anonymous referee for comments which prompted several important clarifications. This paper uses data from the *Infrared Astronomical Satellite*, a joint project of the Netherlands Agency for Aerospace Programs (NIVR), the US National Aeronautics and Space Administration (NASA) and the UK Science and Engineering Research Council (SERC). This publication makes use of data products from the Two Micron All Sky Survey, which is a joint project of the University of Massachusetts and the Infrared Processing and Analysis Center/California Institute of Technology, funded by the National Aeronautics and Space Administration and the National Science Foundation. This research has made use of the NASA/IPAC Infrared Science Archive, which is operated by the Jet Propulsion Laboratory, California Institute of Technology, under contract with the National Aeronautics and Space Administration.

Facilities: Whipple Observatory 1.5-meter (FAST); Whipple Observatory 1.2-meter (STELIRCAM); KPNO 2.1-meter (SQIID and ONIS)

A. Appendix

A.1. IRAS Properties of the BGK and SSM Samples

Differences in the selection of samples of close pairs can have a marked effect on the global properties of the ensemble of galaxies. The BGK and SSM samples are an interesting case of selection in very different wavelength ranges and with different separation criteria. The BGK sample is selected from a complete magnitude limited redshift survey based on the Zwicky et al. (1961-1968) catalog. As a result of the construction of the Zwicky catalog, the BGK sample is deficient in pairs separated by $\leq 5h^{-1}$ kpc. The SSM sample is flux limited at $60\ \mu\text{m}$. The restrictive criterion of projected pairwise separation to three average projected galaxy diameters biases the sample against widely separated pairs. Fig. 14 shows the difference in the distribution of projected pairwise separations for the two samples.

Fig. 15 shows that the SSM sample spans a somewhat broader range of H band luminosity, and the BGK sample is more narrowly peaked. The mean cz of the SSM sample is $4287\ \text{km s}^{-1}$; for BGK, it is $5852\ \text{km s}^{-1}$ explaining the concentration of the BGK distribution toward greater H luminosities. Very low luminosity objects appear predominantly in the SSM sample because BGK have a lower redshift cutoff of $2300\ \text{km s}^{-1}$ which eliminates these objects. We take $H_o = 73\ \text{km s}^{-1}\ \text{Mpc}^{-1}$ for all luminosity comparisons.

Fig. 16 shows that the range of $\log(L_{FIR})$ in the SSM sample is 9.1-11.8; in the BGK sample, the range is 9.3-11.4. As in Fig. 15, the core of the SSM luminosity distribution is broader. The $\langle \log(L_{FIR}) \rangle$ in the SSM sample is 10.5 whereas in the BGK sample $\langle \log(L_{FIR}) \rangle$ is 10.2. The shift toward a broader distribution with a greater $\langle \log(L_{FIR}) \rangle$ in the SSM sample is as expected for an IRAS-selected sample relative to a B-selected sample. Neither sample contains ultraluminous infrared galaxies.

Fig. 17 shows the distributions of $\log L_{FIR}/L_H$, a measure of the normalized star formation rate, for both the SSM and BGK samples. L_{FIR} is directly proportional to the star formation rate (Kennicutt 1988; Calzetti et al. 2000; Charlot et al. 2002; Kewley et al. 2002) and L_H is roughly proportional to the stellar mass. Some investigators use L_K to normalize star formation rates. As we have discussed, L_K is affected by thermal emission from hot dust in these systems and thus L_H is a preferable proxy for the stellar mass.

In Fig. 17, L_H is the H-band luminosity for the pair derived from 2MASS photometry.

Other investigators have shown that the IRAS luminosities of close pairs are frequently dominated by one of the galaxies. In the BGK sample, nearly all of the pairs are unresolved in IRAS and we have no way of knowing the detailed origin of the IRAS emission. We thus normalize the IRAS luminosity by the total H-band luminosity for the pair. This approach may systematically underestimate the normalized star formation rate, but because most pairs are galaxies of comparable H-band luminosity, the bias is of order a factor of 2.

The difference in the distributions is more pronounced in Fig. 17 than in Figure 16. The IRAS selection yields a sample rich in pairs with $\log L_{\text{FIR}}/L_{\text{H}} \geq 2.8$. These objects are too faint at B to be included in the BGK sample. The tail at $\log L_{\text{FIR}}/L_{\text{H}} \leq 1$ in the SSM sample consist of low redshift objects absent by construction from the BGK sample.

The SSM IRAS selected pairs also contain somewhat hotter dust than the BGK pairs detected by IRAS. Figure 18 shows the distributions of F_{60}/F_{100} for both samples. The median temperature of the BGK pairs is 45K; the median for the SSM pairs is 50K.

In general, the BGK sample contains less extreme objects than the SSM sample, but the overlap is substantial over two orders of magnitude in both L_{FIR} and $L_{\text{FIR}}/L_{\text{H}}$. Not surprisingly, pairs with $\log L_{\text{FIR}}/L_{\text{H}} \geq 2.8$ are rare in a B-selected sample like BGK.

REFERENCES

Aaronson, M. 1977, Ph.D. Thesis,

Allam, S. S., Tucker, D. L., Smith, J. A., Lee, B. C., Annis, J., Lin, H., Karachentsev, I. D., & Laubscher, B. E. 2004, AJ, 127, 1883

Alonso, M. S., Tissera, P. B., Coldwell, G., & Lambas, D. G. 2004, MNRAS, 352, 1081

Alonso-Herrero, A., et al. 2006, ApJ, 640, 167

Arp, H. C., & Madore, B. 1987, Cambridge ; New York : Cambridge University Press, 1987.,

Balog, Z., Kenyon, S. J., Lada, E. A., Barsony, M., Vinkó, J., & Gáspár, A. 2004, AJ, 128, 2942

Barsony, M., Kenyon, S. J., Lada, E. A., & Teuben, P. J. 1997, ApJS, 112, 109

Barton, E. J., Geller, M. J., & Kenyon, S. J. 2000, ApJ, 530, 660 (BGK)

Barton Gillespie, E., Geller, M. J., & Kenyon, S. J. 2003, ApJ, 582, 668 (BGK2)

Bekki, K., & Couch, W. J. 2001, ApJ, 557, L19

Bell, E. F., et al. 2006, ApJ, 640, 241

Bessell, M. S., & Brett, J. M. 1988, PASP, 100, 1134

Bragg, A. E., & Kenyon, S. J. 2002, AJ, 124, 3289

Bushouse, H. A., & Werner, M. W. 1990, ApJ, 359, 72

Bushouse, H. A., Werner, M. W., & Lamb, S. A. 1988, ApJ, 335, 74

Calzetti, D., Armus, L., Bohlin, R. C., Kinney, A. L., Koornneef, J., & Storchi-Bergmann, T. 2000, ApJ, 533, 682

Campbell, A. W., & Terlevich, R. 1984, MNRAS, 211, 15

Carico, D. P., Soifer, B. T., Beichman, C., Elias, J. H., Matthews, K., & Neugebauer, G. 1986, AJ, 92, 1254

Charlot, S., Kauffmann, G., Longhetti, M., Tresse, L., White, S. D. M., Maddox, S. J., & Fall, S. M. 2002, MNRAS, 330, 876

Conselice, C. J., et al. 2004, ApJ, 600, L139

Corbett, E. A., et al. 2003, *ApJ*, 583, 670

Cutri, R. M., & McAlary, C. W. 1985, *ApJ*, 296, 90

Devereux, N. A. 1989, *ApJ*, 346, 126

Donzelli, C. J., & Pastoriza, M. G. 1997, *ApJS*, 111, 181

Elias, J. H., Frogel, J. A., Matthews, K., & Neugebauer, G. 1982, *AJ*, 87, 1029

Falco, E. E., et al. 1999, *PASP*, 111, 438

Ferland, G. J., 1980, *PASP*, 92, 596

Fruchter, A. S., & Hook, R. N. 2002, *PASP*, 114, 144

Gallagher, J. S., & Smith, L. J. 1999, *MNRAS*, 304, 540

Geller, M. J., & Huchra, J. P. 1989, *Science*, 246, 897

Giovanelli, R., & Haynes, M. P. 1985, *AJ*, 90, 2445

Giovanelli, R., & Haynes, M. P. 1989, *AJ*, 97, 633

Giovanelli, R., & Haynes, M. P. 1993, *AJ*, 105, 1271

Giovanelli, R., Myers, S. T., Roth, J., & Haynes, M. P. 1986, *AJ*, 92, 250

Giuricin, G., Biviano, A., Girardi, M., Mardirossian, F., & Mezzetti, M. 1993, *A&A*, 275, 390

Glass, I. S., & Moorwood, A. F. M. 1985, *MNRAS*, 214, 429

Gómez, M., & Kenyon, S. J. 2001, *AJ*, 121, 974

Goto, T. 2005, *MNRAS*, 360, 322

Griersmith, D., Hyland, A. R., & Jones, T. J. 1982, *AJ*, 87, 1106

Guiderdoni, B., Hivon, E., Bouchet, F. R., & Maffei, B. 1998, *MNRAS*, 295, 877

Haynes, M. P., Magri, C., Giovanelli, R., & Starosta, B. M. 1988, *AJ*, 95, 607

Helou, G., Khan, I. R., Malek, L., & Boehmer, L. 1988, *ApJS*, 68, 151

Helou, G., Lu, N. Y., Werner, M. W., Malhotra, S., & Silbermann, N. 2000, *ApJ*, 532, L21

Huchra, J. P., Geller, M. J., & Corwin, H. G. 1995, *ApJS*, 99, 391

Huchra, J. P., Vogeley, M. S., & Geller, M. J. 1999, *ApJS*, 121, 287

Hunt, L. K., Giovanardi, C., & Helou, G. 2002, *A&A*, 394, 873

IRAS Catalogs and Atlases: Explanatory Supplement to the IRAS Point Source Catalog 1985, edited by C. Beichman et al. GPO, Washington, DC

Jansen, R. A., Franx, M., Fabricant, D., & Caldwell, N. 2000a, *ApJS*, 126, 271

Jansen, R. A., Fabricant, D., Franx, M., & Caldwell, N. 2000b, *ApJS*, 126, 331

Jarrett, T. H. 2000, *PASP*, 112, 1008

Jarrett, T. H., Chester, T., Cutri, R., Schneider, S., Skrutskie, M., & Huchra, J. P. 2000, *AJ*, 119, 2498

Jones, B., & Stein, W. A. 1989, *AJ*, 98, 1557

Kassin, S. A., Frogel, J. A., Pogge, R. W., Tiede, G. P., & Sellgren, K. 2003, *AJ*, 126, 1276

Keel, W. C. 1993, *Revista Mexicana de Astronomia y Astrofisica*, vol. 27, 27, 77

Keel, W. C., & Borne, K. D. 2003, *AJ*, 126, 1257

Kennicutt, R. C. 1998, *ARA&A*, 36, 189

Kennicutt, R. C., & Keel, W. C. 1984, *ApJ*, 279, L5

Kennicutt, R. C., Roettiger, K. A., Keel, W. C., van der Hulst, J. M., & Hummel, E. 1987, *AJ*, 93, 1011

Kewley, L. J., Dopita, M. A., Sutherland, R. S., Heisler, C. A., & Trevena, J. 2001, *ApJ*, 556, 121

Kewley, L. J., Geller, M. J., Jansen, R. A., & Dopita, M. A. 2002, *AJ*, 124, 3135

Kewley, L. J., Geller, M. J., & Barton, E. J. 2005, ArXiv Astrophysics e-prints, arXiv:astro-ph/0511119

Kewley, L. J., Heisler, C. A., Dopita, M. A., & Lumsden, S. 2001, *ApJS*, 132, 37

Kewley, L. J., Jansen, R. A., & Geller, M. J. 2005, *PASP*, 117, 227

Lambas, D. G., Tissera, P. B., Alonso, M. S., & Coldwell, G. 2003, *MNRAS*, 346, 1189

Larios, G. R., & Phillips, J. P. 2005, MNRAS, 357, 732

Larson, R. B., & Tinsley, B. M. 1978, ApJ, 219, 46

Lavalley, M., Isobe, T., & Feigelson, E. 1992, ASP Conf. Ser. 25: Astronomical Data Analysis Software and Systems I, 25, 245

Lin, L., et al. 2004, ApJ, 617, L9

Liu, C. T., & Kennicutt, R. C. 1995, ApJS, 100, 325

Liu, C. T., & Kennicutt, R. C. 1995, ApJ, 450, 547

López-Sánchez, Á. R., Esteban, C., & Rodríguez, M. 2004, ApJS, 153, 243

Marzke, R. O., Geller, M. J., da Costa, L. N., & Huchra, J. P. 1995, AJ, 110, 477

Mihos, J. C., & Hernquist, L. 1996, ApJ, 464, 641

Mihos, J. C., Richstone, D. O., & Bothun, G. D. 1991, ApJ, 377, 72

Moorwood, A. F. M., Veron-Cetty, M.-P., & Glass, I. S. 1987, A&A, 184, 63

Nikolaev, S., Weinberg, M. D., Skrutskie, M. F., Cutri, R. M., Wheelock, S. L., Gizis, J. E., & Howard, E. M. 2000, AJ, 120, 3340

Nikolic, B., Cullen, H., & Alexander, P. 2004, MNRAS, 355, 874

Papovich, C., Dickinson, M., Giavalisco, M., Conselice, C. J., & Ferguson, H. C. 2005, ApJ, 631, 101

Patton, D. R., Carlberg, R. G., Marzke, R. O., Pritchett, C. J., da Costa, L. N., & Pellegrini, P. S. 2000, ApJ, 536, 153

Patton, D. R., et al. 2002, ApJ, 565, 208

Poggianti, B. M. 1997, A&AS, 122, 399

Press, W. H., Teukolsky, S. A., Vetterling, W. T., & Flannery, B. P. 1992, Cambridge: University Press, —c1992, 2nd ed.,

Sanders, D. B., & Mirabel, I. F. 1996, ARA&A, 34, 749

Sekiguchi, K., & Wolstencroft, R. D. 1992, MNRAS, 255, 581

Skrutskie, M. F., et al. 2006, AJ, 131, 1163

Smith, D. A., Herter, T., Haynes, M. P., Beichman, C. A., & Gautier, T. N. 1996, ApJS, 104, 217

Stanford, S. A., Stern, D., van Breugel, W., & De Breuck, C. 2000, ApJS, 131, 185

Surace, J. A., Sanders, D. B., & Mazzarella, J. M. 2004, AJ, 127, 3235

Telesco, C. M., Wolstencroft, R. D., & Done, C. 1988, ApJ, 329, 174

Veilleux, S., Kim, D.-C., Sanders, D. B., Mazzarella, J. M., & Soifer, B. T. 1995, ApJS, 98, 171

Wegner, G., Haynes, M. P., & Giovanelli, R. 1993, AJ, 105, 1251

Whitelock, P. A. 1985, MNRAS, 213, 59

Whitney, B. A., Kenyon, S. J., & Gomez, M. 1997, ApJ, 485, 703

Zwicky, F. et al. 1961-68, *Catalog of Galaxies and of Clusters of Galaxies*, Pasadena: California Institute of Technology (CIT),

Table 1. 2MASS Infrared Photometry

J2000 Designation	Redshift	7" aperture			Isophotal aperture			Split
		J	H	K	J	H	K	
08042396+2930516	5447	13.87	13.22	12.90	13.51	12.91	12.60	
08042496+2930236	5298	12.11	11.40	11.15	11.80	11.12	10.87	
08065208+1844155	4557	12.03	11.32	11.05	11.72	11.02	10.74	
08070665+1845506	4661	13.98	13.46	13.18	13.62	13.02	12.76	
08100603+2455194	4128	12.70	11.97	11.71	12.19	11.47	11.24	
08101117+2453344	4089	14.36	13.76	13.51	13.72	13.11	12.80	
08111348+2512249	3995	12.82	12.10	11.80	11.35	10.66	10.40	
08111591+2510459	4039	13.15	12.53	12.27	12.79	12.18	11.88	
08112548+0853382	5763	14.09	13.45	13.15	14.31	13.66	13.34	+
08112703+0856280	5704	14.00	13.32	13.05	13.86	13.19	12.97	

*Full table appears in the electronic edition

Table 2. Journal of Observations

UT Date	Telescope	IR Imager	Field of View
13 Mar 2000–20 Mar 2000	1.2-m	STELIRCAM	300"× 300"
23 Mar 2000–26 Mar 2000	2.1-m	ONIS	175"× 350"
15 Oct 2000–18 Oct 2000	2.1-m	SQIID	300"× 300"
8 Apr 2001–12 Apr 2001	1.2-m	STELIRCAM	300"× 300"
26 Sep 2001–27 Sep 2001	1.2-m	STELIRCAM	300"× 300"
6 Oct 2001–9 Oct 2001	2.1-m	SQIID	300"× 300"
3 Mar 2002–5 Mar 2002	1.2-m	STELIRCAM	300"× 300"
21 Oct 2002–23 Mar 2002	1.2-m	STELIRCAM	300"× 300"

Table 3. BGK Infrared Photometry

J2000 Designation	L (arcsec)	w (arcsec)	PA (deg)	J	H	K
08042396+2930516	38.4	3.0	90.0	14.12	13.54	13.16
08042496+2930236	4.0	3.0	90.0	13.28	12.60	12.34
08065208+1844155	16.8	3.0	90.0	12.53	11.82	11.58
08070665+1845506	28.3	3.0	90.0	14.90	14.28	14.03
08111348+2512249	12.2	3.0	90.0	13.53	12.84	12.58
08111591+2510459	28.8	3.0	90.0	13.87	13.22	13.03
08112548+0853382	26.4	3.0	90.0	14.87	14.38	14.05
08112703+0856280	28.8	3.0	90.0	14.32	13.62	13.41
08184909+2113053	19.1	3.0	90.0	14.69	14.01	13.84
08190189+2111093	4.3	3.0	90.0	15.31	14.58	14.35

*Full table appears in the electronic edition

Table 4. IRAS Mid-Infrared Photometry

J2000 Designation	IRAS Designation	Fluxes in Jy			
		12 μ m	25 μ m	60 μ m	100 μ m
08042396+2930516	08012+2939	0.25L	0.37L	0.43	1.10L
08042496+2930236	08012+2939	0.25L	0.37L	0.43	1.10L
08100603+2455194	08070+2503	0.48L	0.31L	0.93	1.13:
08101117+2453344	08070+2503	0.48L	0.31L	0.93	1.13:
08111348+2512249	08082+2521	0.25L	0.46L	2.14	5.97
08111591+2510459	08082+2521	0.25L	0.46L	2.14	5.97
08184909+2113053	08161+2120	0.25L	0.61L	0.54:	1.51
08190189+2111093	08161+2120	0.25L	0.61L	0.54:	1.51
08194129+2202311	08168+2211	0.25L	0.34L	0.74	2.12
08194833+2201531	08168+2211	0.25L	0.34L	0.74	2.12

*Full table appears in the electronic edition

^aTo preserve associations of IRAS detections with pair galaxies, we list IRAS associations for each galaxy in the pair. This listing duplicates flux measurements for pair galaxies where IRAS could not spatially resolve the pair. For the IRAS fluxes, 'L' indicates an upper limit (quality flag 1), and ':' indicates an approximate flux (quality flag 2).

Table 5. BGK Pairs Brighter than Surace Flux Limits

Pair ID	IRAS ID	F_{12} (Jy)	F_{25} (Jy)	F_{60} (Jy)	F_{100} (Jy)
011934.70+032445.22	01171+0308	0.56:	1.10	6.41	12.24
023726.83+210716.52	02345+2053	0.56	1.22	10.18	16.93
091549.24+405355.59	09120+4107	0.52	1.07	8.75	16.60
160513.04+203230.75	16030+2040	0.24:	0.87	7.04	10.10

Table 6. JHK Model Parameters

Model Number	$(J-H)_0$	$(H-K)_0$	σ_{J-H}	σ_{H-K}	σ_B	σ_D	σ_G	σ_R
R	0.67	0.27	0.05	0.05	0.00	0.000	0.00	0.020
B	0.67	0.27	0.05	0.05	0.05	0.000	0.00	0.020
G	0.67	0.27	0.05	0.05	0.00	0.000	0.05	0.020
BGK	0.72	0.20	0.06	0.06	0.08	0.008	0.04	0.06

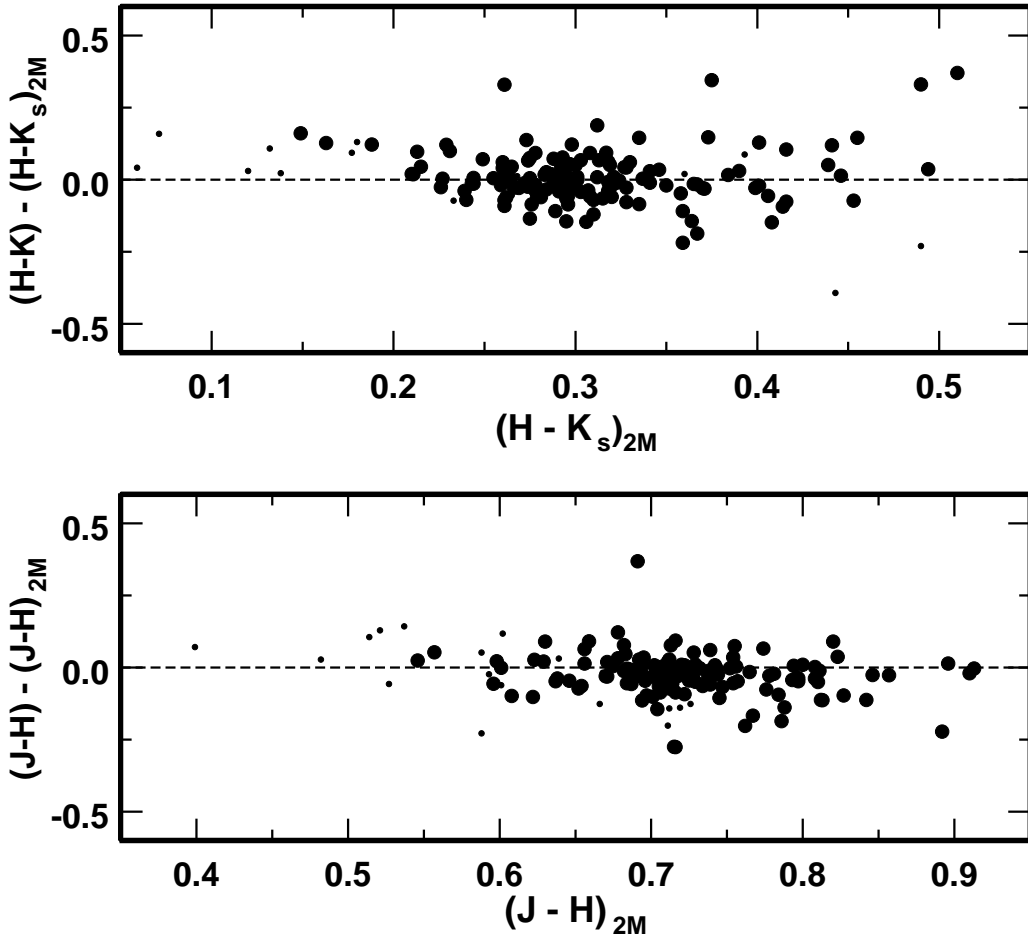


Fig. 1.— Comparison of our slit aperture ($J-H$) and ($H-K$) photometry with 2MASS 7'' diameter aperture ($H-K_s)_{2M}$ (top) and $(J-H)_{2M}$ (bottom). The small points are galaxies with 2MASS isophotal $J > 13$. The error in our colors is 0.04 mag; the error in the 2MASS colors is 0.03 mag. The dispersion in the relative colors is consistent with these errors.

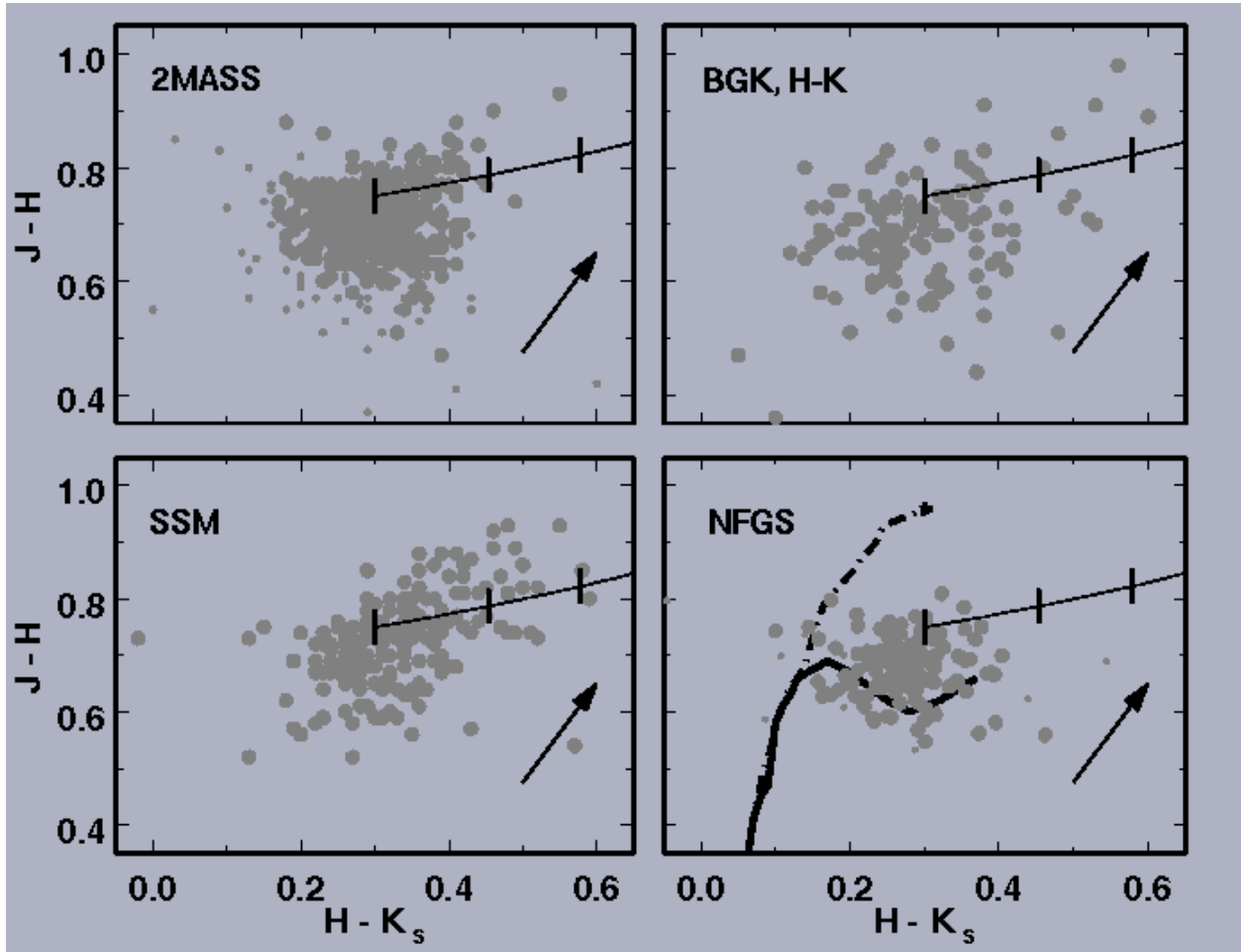


Fig. 2.— Near infrared color-color diagrams for the BGK sample 2MASS data (upper left), the BGK small aperture JHK data (upper right, this paper), SSM pair 2MASS data (lower left), NFGS “normal” galaxy 2MASS data (lower right). Note the large spread of colors in the pair samples relative to the NFGS. The small points denote galaxies with $J > 13$; these objects tend to be blue as a result of the original B-selected sample. In each panel the arrow shows the reddening vector, the curve with ticks shows the fractional contribution of 1000K dust at K; each tick marks a 10% increment. In the NFGS panel, the curves show the color of main sequence stars (solid) and the giant branch (dot-dashed) from Bessel and Brett (1988).

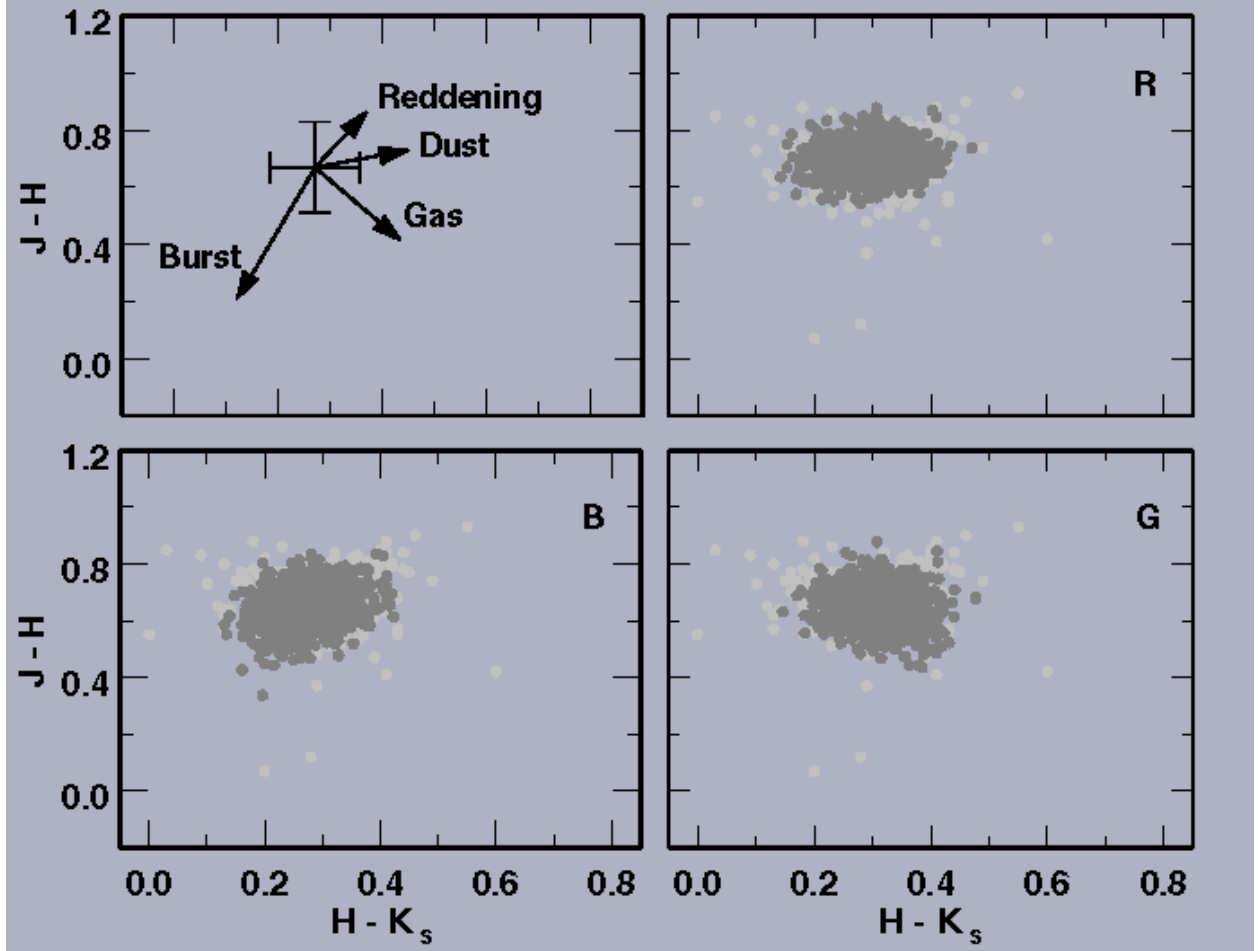


Fig. 3.— Heuristic statistical model for the 2MASS BGK pairs color-color diagram. The upper left panel is a schematic showing the physical components of the model. The cross indicates the colors of a “normal” galaxy population. The arrows show the direction a galaxy moves in this color space as a result of reddening, hot dust emission, gaseous emission, and young bursts as indicated. In the other three panels gray points show the data; black points show the model. In the upper right, the model (R, Table 6) contains only the scatter in colors and reddening; in the lower left we add bursts of star formation emission (B; Table 6) and on the lower right we add gaseous emission (G; Table 6). Table 6 gives the model parameters. In each panel, note the change in shape of the central mass of points and the behavior of the outliers. The models account for most of the observed spread of colors.

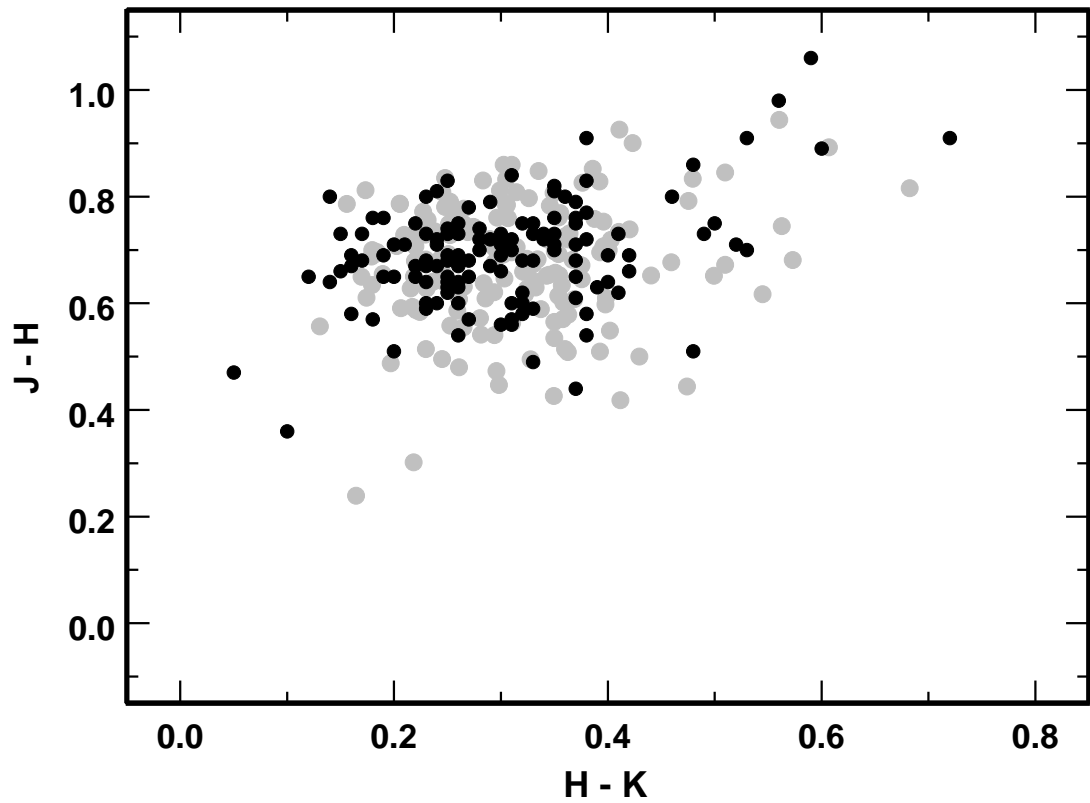


Fig. 4.— Comparison of slit photometry colors for 160 BGK galaxies with the model (parameters in Table 6; BGK). Gray points represent the data; black points show the model. The K-band (as opposed to K_s photometry) is more sensitive to hot dust emission, necessary to account for the reddest objects in H-K.

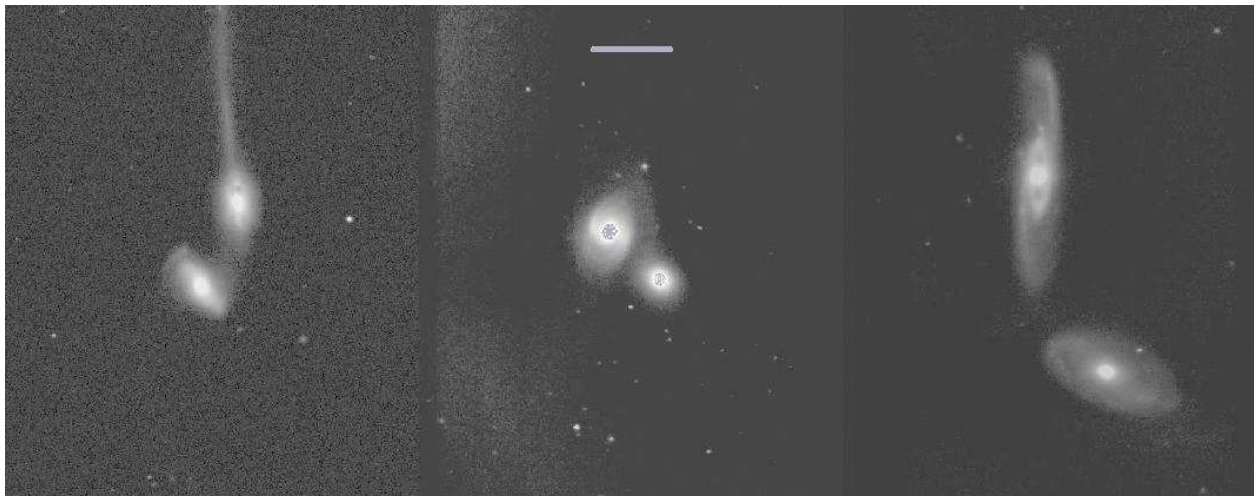


Fig. 5.— Near-infrared images for three galaxy pairs. The images have North up and East to the left and scales of $0.34 \text{ arcsec pixel}^{-1}$. The white bar in the central image has a length of 10 arcsec . (a) Left panel: J-band image of $124344.0+310017.9$ ($H-K = 0.60$) and $124345.3+305943.8$ ($H-K = 0.37$). The northern component has a dust lane on JHK images. (b) Middle panel: K-band image of $152418.9+415040.7$ ($H-K = 0.28$) and $152420.9+415059.5$ ($H-K = 0.72$). The redder eastern component has a tidal tail not visible on the DSS image. (c) Right panel: K-band image of $113704.8+321108.9$ ($H-K = 0.82$) and $113707.1+321227.2$ ($H-K = 0.22$). The southern component is a red AGN which we exclude from the sample; the blue northern component, retained in the sample, has a bright ring of star formation. The $30''$ white bar gives the image scale.

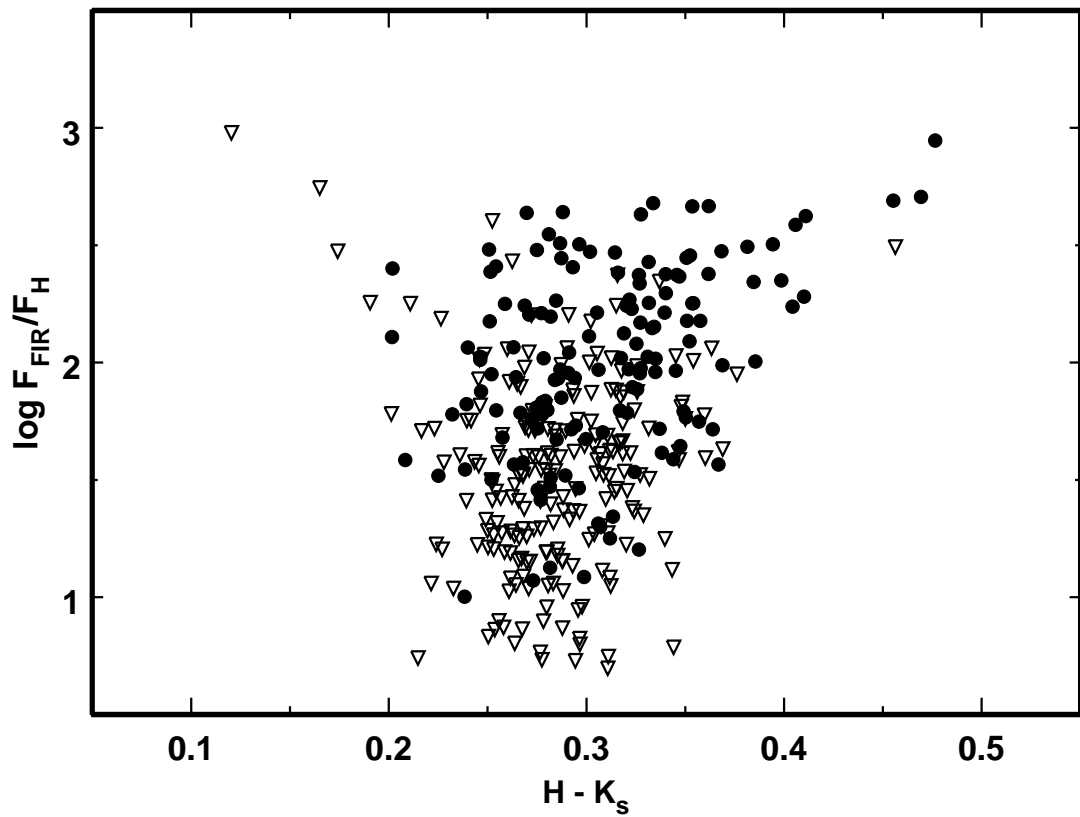


Fig. 6.— $L_{\text{FIR}}/L_{\text{H}}$ for the BGK pairs. The solid points are detections; the open triangles are upper limits.

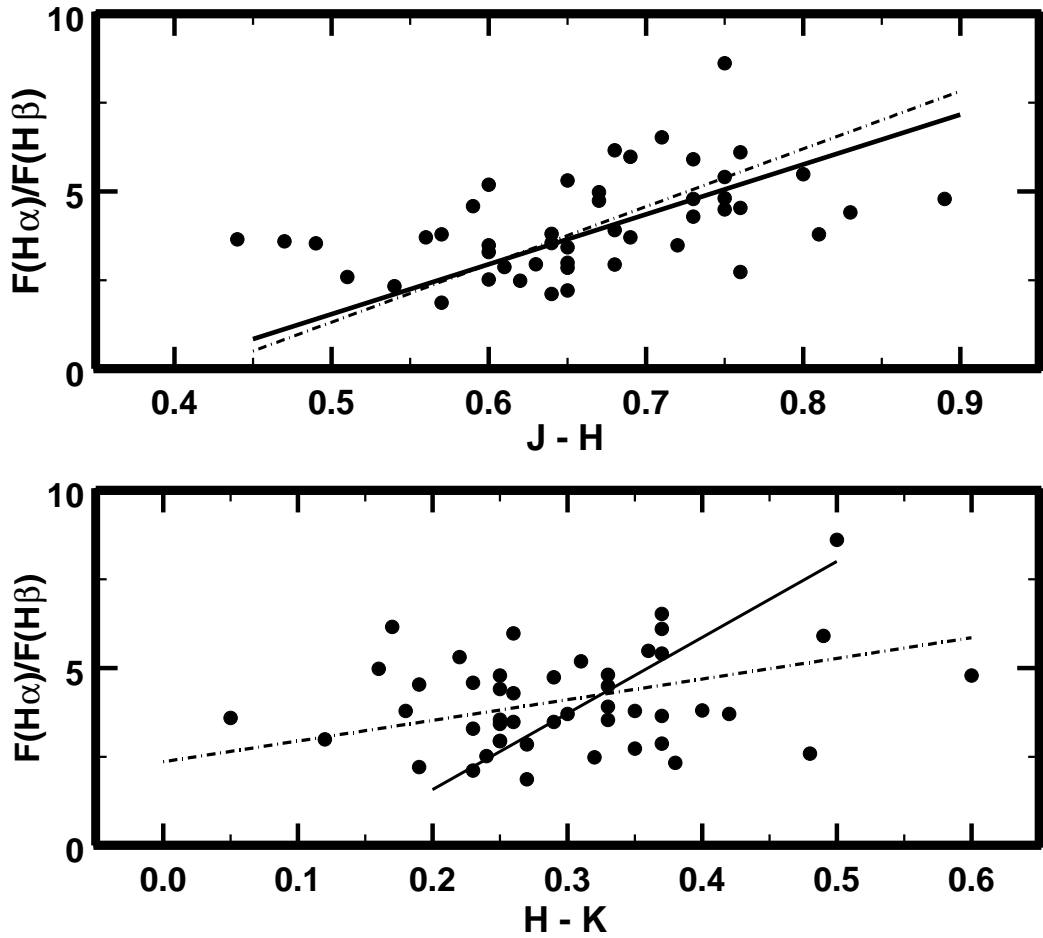


Fig. 7.— Balmer decrement for 45 BGK galaxies as a function of $J-H$ (top) and $H-K$ (bottom). The colors are measured in the spectroscopic aperture. The solid line shows the Galactic reddening law; the dot-dashed lines show the best fit slope. For $J-H$ the fitted slope is essentially the same as the Galactic reddening law; for $H-K$ the slopes differ because hot dust emission affects the $H-K$ color.

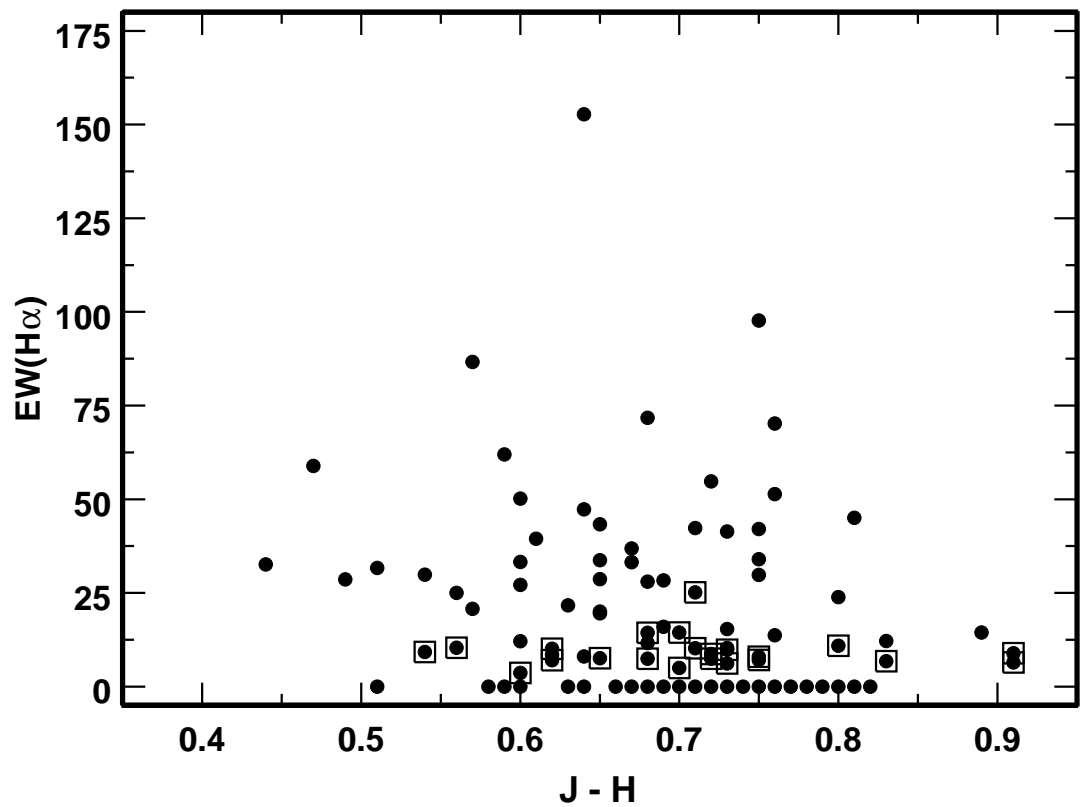


Fig. 8.— Equivalent width of H α as a function of J-H for 151 BGK galaxies. The color is measured in the spectroscopic aperture. Boxes denote galaxies with non-zero EW(H α) but undetectable H β .

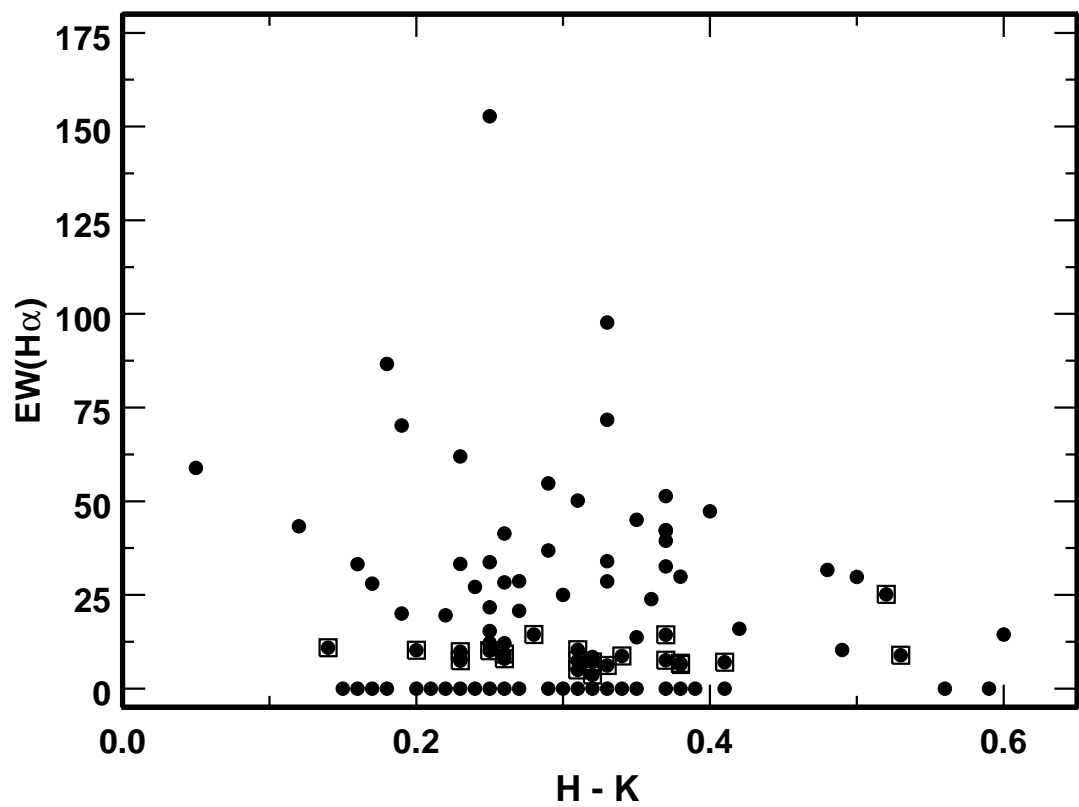


Fig. 9.— Equivalent width of H α as a function of H-K for 151 BGK galaxies. The color is measured in the spectroscopic aperture. Boxes denote galaxies with non-zero EW(H α) but undetectable H β .

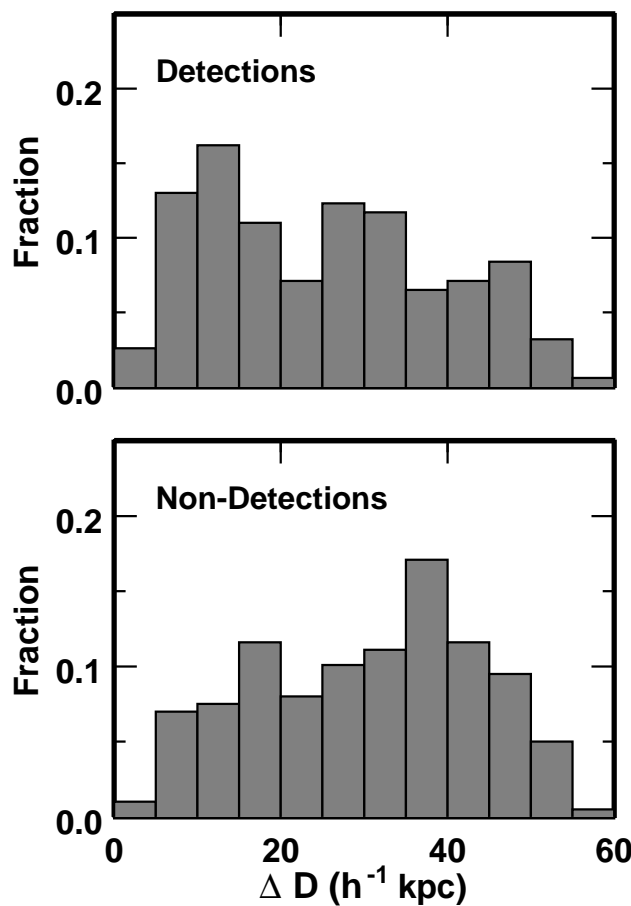


Fig. 10.— Normalized distribution of projected separations for IRAS-detected BGK pairs (top) and undetected pairs (bottom)

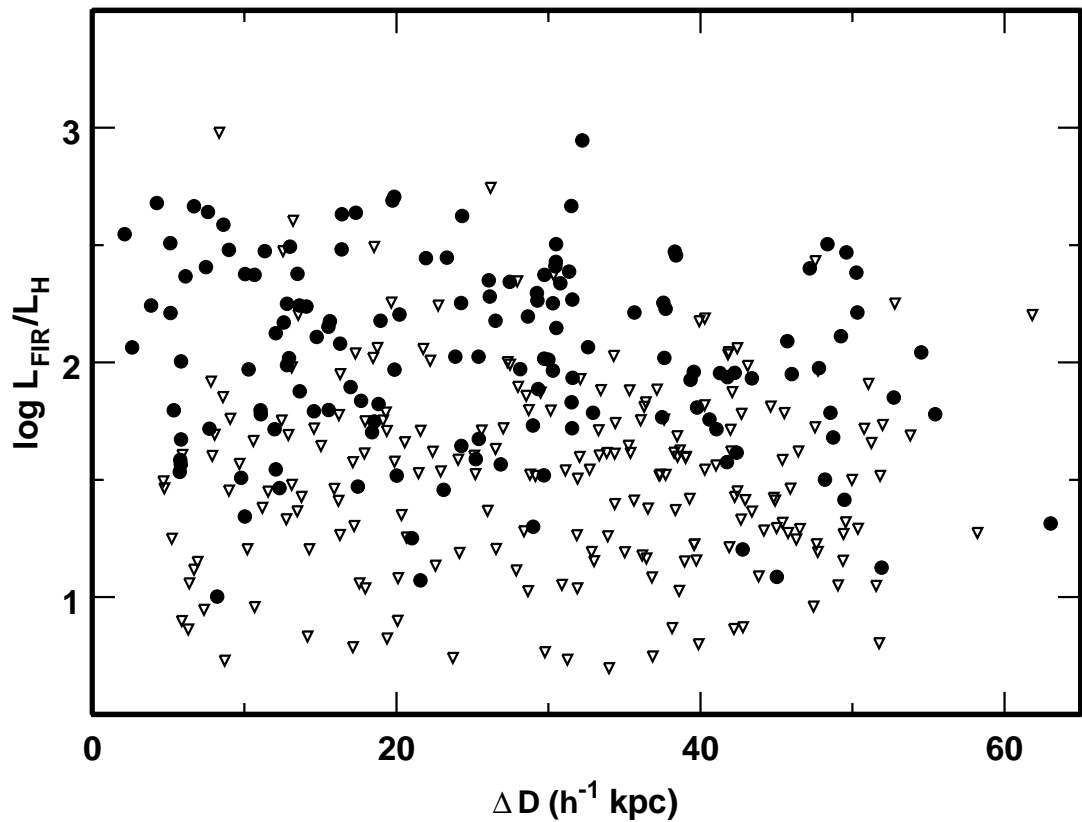


Fig. 11.— $L_{\text{FIR}}/L_{\text{H}}$ as a function of separation for the BGK pairs. Solid dots are detections, open triangles are upper limits. Note that $L_{\text{FIR}}/L_{\text{H}}$ refers to individual pairs, not individual galaxies.

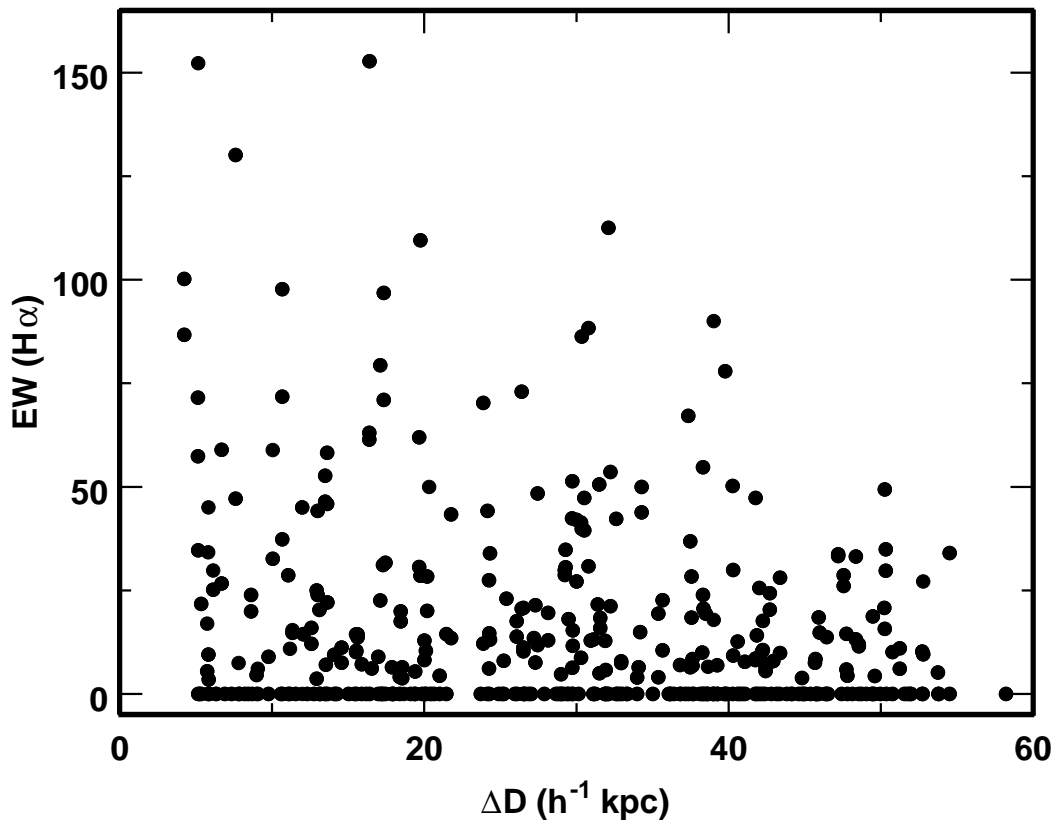


Fig. 12.— EW(H α) as a function of projected separation for BGK pairs. Each point represents an individual galaxy.

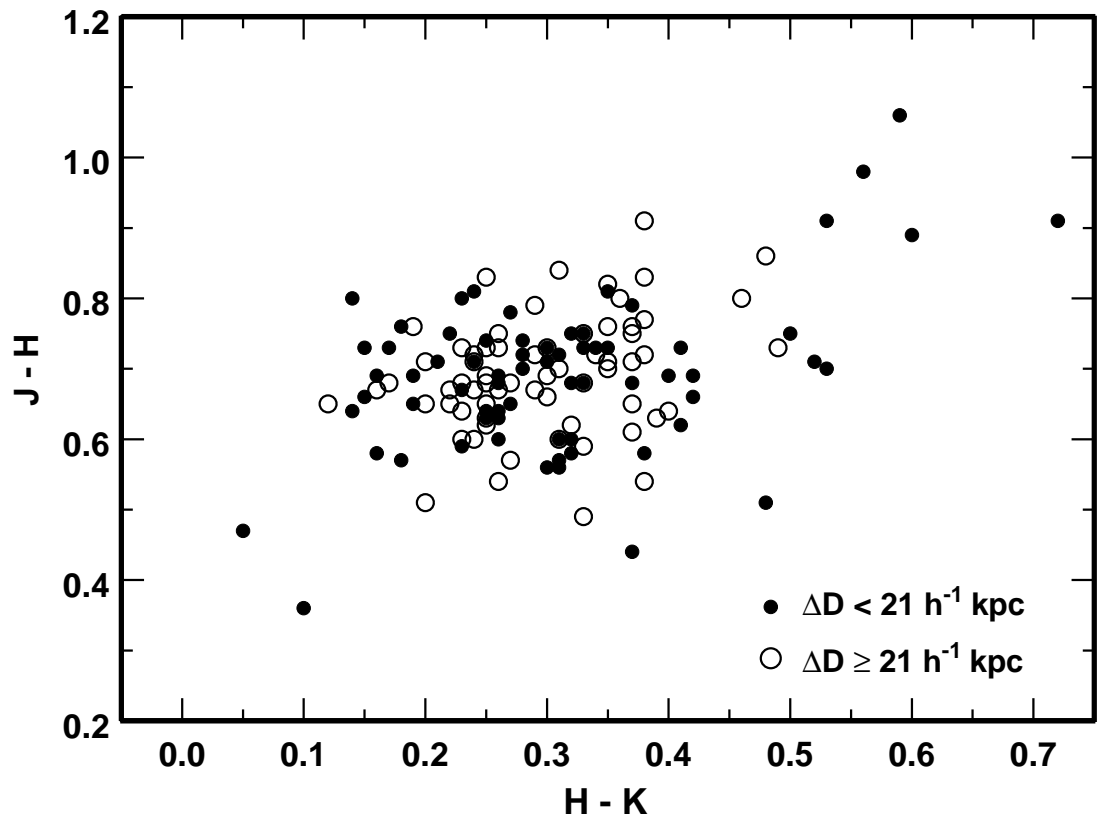


Fig. 13.— Small aperture photometry near infrared color-color diagram for 160 galaxies in BGK pairs with projected separations $\Delta D < 21 h^{-1} \text{ kpc}$ (solid dots) and with projected separation $\Delta D \geq 21 h^{-1} \text{ kpc}$ (open circles).

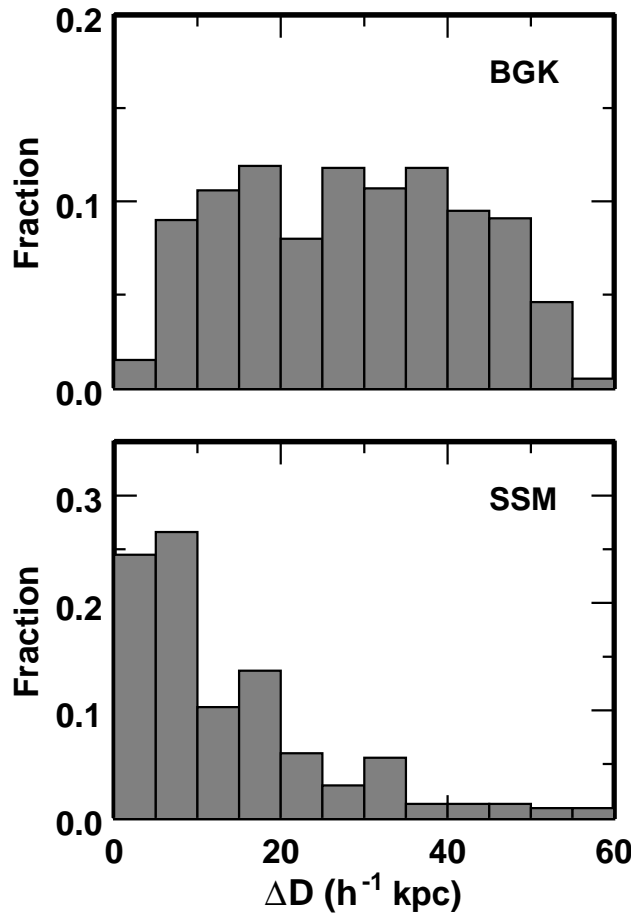


Fig. 14.— Normalized distributions of projected pairwise separations for the BGK and SSM samples.

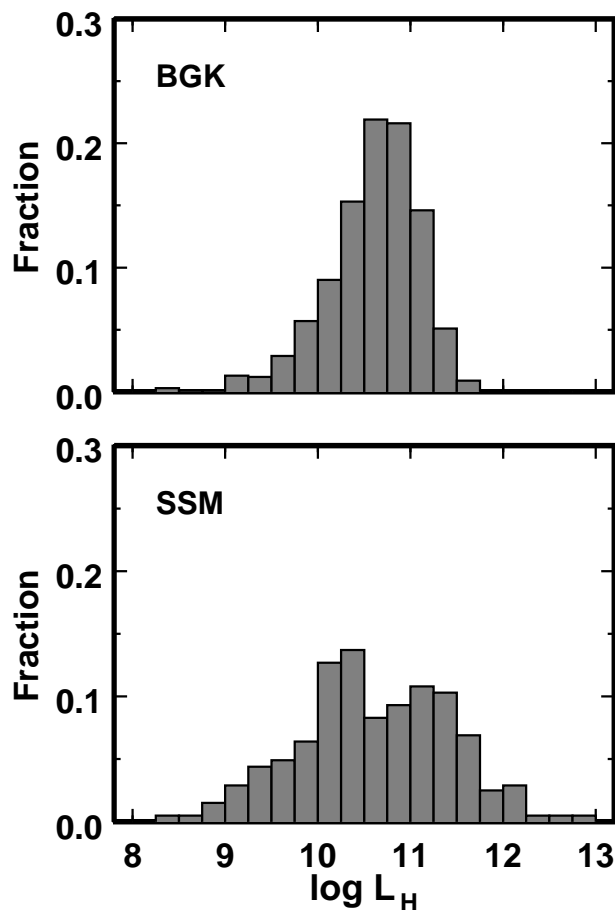


Fig. 15.— Normalized distributions of L_H for *individual galaxies* in the BGK and SSM pair samples. Note the broader distribution of SSM luminosities.

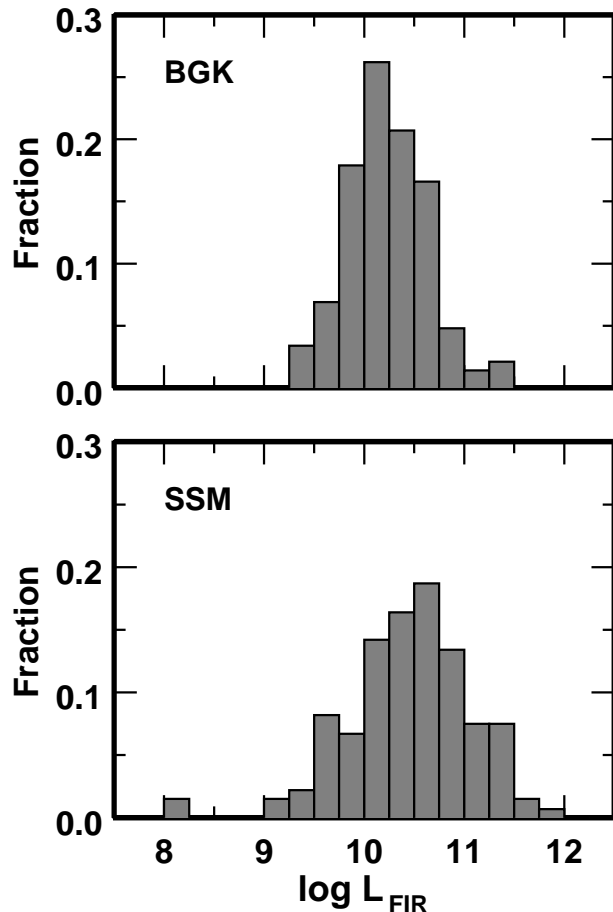


Fig. 16.— Normalized distributions of L_{FIR} for BGK and SSM pairs. Note the extension of the SSM luminosity distribution into the ULIRG range.

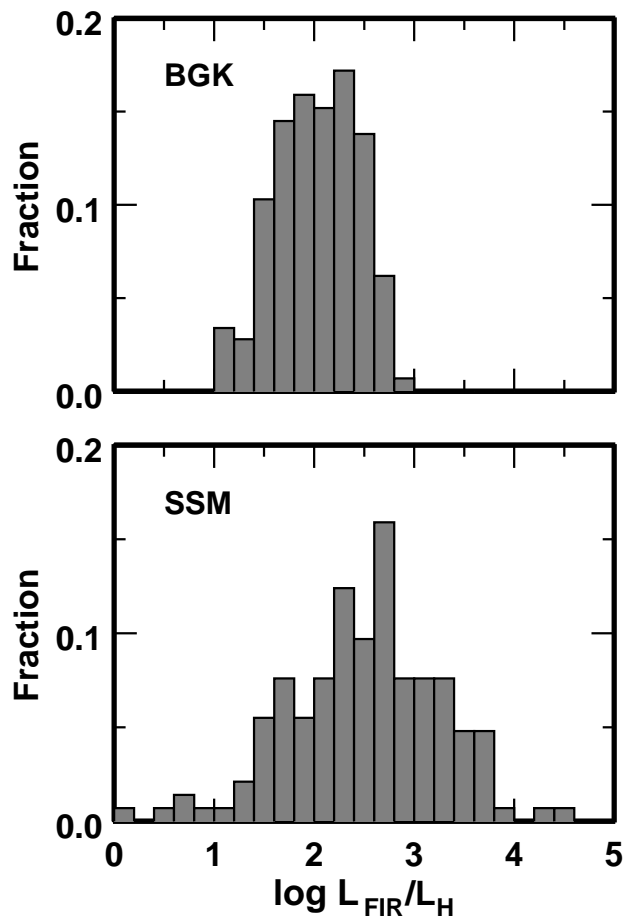


Fig. 17.— Normalized distributions of $L_{\text{FIR}}/L_{\text{H}}$ for the BGK and SSM pairs.

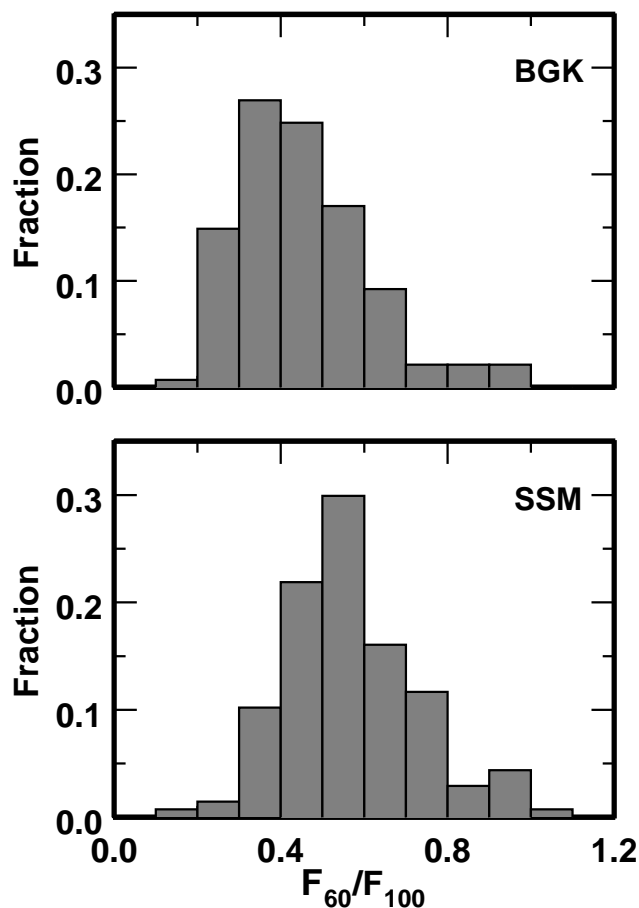


Fig. 18.— Normalized distributions of F_{60}/F_{100} for the BGK and SSM pairs.